



Finite element modeling of linear elastodynamics problems with explicit time-integration methods and linear elements with the reduced dispersion error



A. Idesman*, D. Pham

Department of Mechanical Engineering, Texas Tech University, Lubbock, TX 79409-1021, USA

ARTICLE INFO

Article history:

Received 7 November 2012

Received in revised form 30 November 2013

Accepted 15 December 2013

Available online 3 January 2014

Keywords:

Elastic waves

Numerical dispersion

Explicit time integration

Finite elements

ABSTRACT

We have developed two finite element techniques with reduced dispersion for linear elastodynamics that are used with explicit time-integration methods. These techniques are based on the modified integration rule for the mass and stiffness matrices and on the averaged mass matrix approaches that lead to the numerical dispersion reduction for linear finite elements. The analytical study of numerical dispersion for the new techniques is carried out in the 1-D, 2-D and 3-D cases. The numerical study of the efficiency of the dispersion reduction techniques includes the two-stage time-integration approach with the filtering stage (developed in our previous papers) that quantifies and removes spurious high-frequency oscillations from numerical results. We have found that in contrast to the standard linear elements with explicit time-integration methods and the lumped mass matrix, the finite element techniques with reduced dispersion yield more accurate results at small time increments (smaller than the stability limit) in the 2-D and 3-D cases. The recommendations for the selection of the size of time increments are suggested. The new approaches with reduced dispersion can be easily implemented into existing finite element codes and lead to significant reduction in computation time at the same accuracy compared with the standard finite element formulations.

© 2013 Elsevier B.V. All rights reserved.

1. Introduction

The application of the space discretization to transient acoustics or transient linear elastodynamics problems leads to a system of ordinary differential equations in time

$$\mathbf{M}\ddot{\mathbf{U}} + \mathbf{C}\dot{\mathbf{U}} + \mathbf{K}\mathbf{U} = \mathbf{R}, \quad (1)$$

where \mathbf{M} , \mathbf{C} , \mathbf{K} are the mass, damping, and stiffness matrices, respectively, \mathbf{U} is the vector of the nodal displacement, \mathbf{R} is the vector of the nodal load. Zero viscosity, $\mathbf{C} = \mathbf{0}$, is considered in the paper. Due to the space discretization, the exact solution to Eq. (1) contains the numerical dispersion error; e.g., see [1–14] and others. The space discretization error can be decreased by the use of mesh refinement. However, this procedure significantly increases computational costs. Therefore, special techniques have been developed for the reduction in the numerical dispersion error which is also related to “the pollution effect” (e.g., see [15–17] and others for the study of the pollution error). One simple and efficient technique for acoustic and elastic wave propagation problems is based on the calculation of the mass matrix \mathbf{M} in Eq. (1) as a weighted average of the

* Corresponding author. Tel.: +1 806 742 3563; fax: +1 806 742 3540.

E-mail address: alexander.idesman@ttu.edu (A. Idesman).

consistent and lumped mass matrices; see [5–8] and others. For the 1-D case and linear finite elements, this approach reduces the error in the wave velocity for harmonic waves from the second order to the fourth order of accuracy. However, for harmonic wave propagation in the 2-D and 3-D cases, these results are not valid (nevertheless, in the multidimensional case, the averaged mass matrix yields more accurate results compared with the standard mass matrix; e.g., see the numerical results in Section 3). We should also mention that the known publications on the techniques with the averaged mass matrix do not include the effect of finite time increments on the dispersion error and on the accuracy of the numerical results. As shown in the current paper, if we use the weighting coefficients for the averaged mass matrix that are independent of time increments (as in the known approaches) and if the time increments for explicit time-integration methods are close to the stability limit then there is no advantages in the use of the averaged mass matrix compared with the lumped mass matrix.

An interesting technique with implicit and explicit time-integration methods is suggested in [10] for acoustic waves in the 2-D case. It is based on the modified integration rule for the calculation of the mass and stiffness matrices for linear finite elements. In contrast to the averaged mass matrix, the use of the modified integration rule increases the accuracy for the phase velocity from the second order to the fourth order in the general multi-dimensional case of acoustic waves. However, the applicability of this technique to elastodynamics problems has not been studied. The technique in [10] has not treated spurious oscillations that may significantly destroy the accuracy of numerical results.

We should mention that the analysis of numerical dispersion estimates the numerical error for propagation of harmonic waves. In the general case of loading (boundary conditions), the estimation of the accuracy of numerical techniques with reduced dispersion is difficult due to the presence of spurious high-frequency oscillations in numerical solutions; e.g., see [3,5].

In our previous paper [18], we have described the finite element techniques with reduced dispersion for elastodynamics that are based on implicit time-integration methods with very small time increments. These techniques significantly reduce the computation time at the same accuracy compared with the standard finite element formulations with the consistent mass matrix. However, one of the disadvantages of the use of implicit time-integration methods is the necessity to solve a system of algebraic equations that can require large computational resources for a large number of degrees of freedom. In this paper we have extended the finite element techniques with reduced dispersion that can be used with explicit time-integration methods. We have considered two techniques: one of them is based on the use of the averaged mass matrix; another is based on the modified integration rule for the mass and stiffness matrices. In contrast to our paper [18], in the present paper we have also studied the effect of time increments on the dispersion error and on the accuracy of the numerical results.

The paper consists of a modification of the system of semidiscrete equations, Eq. (1), that can be used with explicit time-integration methods and the finite elements with reduced dispersion (Section 2), the analytical study of numerical dispersion for the modified integration rule and for the averaged mass matrix techniques that are used with the 1-D, 2-D and 3-D linear finite elements and the explicit time-integration method (Section 2), a short description of the two-stage time-integration technique with the filtering of spurious oscillations that is suggested in our previous papers [18–23] (Appendix), and 1-D, 2-D and 3-D numerical examples showing the efficiency of the new technique with reduced dispersion (Section 3).

2. Dispersion analysis

In this section, we will develop the averaged mass matrix technique and the modified integration rule technique that are used with explicit time-integration methods. These two techniques significantly reduce the numerical dispersion error and the computation time compared with the standard finite element formulations for linear elastodynamics. In contrast to the study of the averaged mass matrix technique and the modified integration rule technique for the scalar wave equation considered in [5,10], the analytical study of these techniques for elastodynamics problems is much more complicated due to a greater number of non-linear terms in the dispersion equation for elastodynamics and the presence of two different types of waves (compressional and shear waves). Similar to the paper [5], we will first modify Eq. (1) for the use of explicit time-integration methods (for simplicity we assume that the damping matrix is zero, $\mathbf{C} = \mathbf{0}$). Let's rewrite Eq. (1) with the diagonal (lumped) mass matrix \mathbf{D} as follows

$$\mathbf{D}\dot{\mathbf{V}} + \mathbf{KU} = \mathbf{R}, \quad (2)$$

where \mathbf{V} is the vector of nodal velocity. Relationships between the nodal displacements and velocities can be written down as (similar to those in [5,10])

$$\mathbf{D}\dot{\mathbf{U}} = \mathbf{MV} \quad \text{or} \quad \mathbf{D}\ddot{\mathbf{U}} = \mathbf{M}\dot{\mathbf{V}}, \quad (3)$$

where \mathbf{M} is the non-diagonal mass matrix calculated by the averaged mass matrix technique (see Eq. (8) below) or by the modified integration rule technique (see Eqs. (9), (11) and (13) below). Premultiplying Eq. (2) by \mathbf{MD}^{-1} and inserting Eq. (3) into Eq. (2) we will get

$$\mathbf{D}\ddot{\mathbf{U}} + \mathbf{MD}^{-1}\mathbf{KU} = \mathbf{MD}^{-1}\mathbf{R}. \quad (4)$$

Eq. (4) differs from the standard finite element equations with the lumped mass matrix by the stiffness matrix and the load vector which are multiplied by the term $\mathbf{M}\mathbf{D}^{-1}$. For the time integration of Eq. (4) we will use the standard explicit central-difference method (the most popular explicit method); e.g., see [22,24,25]. Replacing the second time derivative in Eq. (4) by the corresponding finite difference approximation used in the central-difference method, we obtain

$$\mathbf{D}[\mathbf{U}(t + \Delta t) - 2\mathbf{U}(t) + \mathbf{U}(t - \Delta t)]/\Delta t^2 + \mathbf{M}\mathbf{D}^{-1}\mathbf{K}\mathbf{U}(t) = \mathbf{M}\mathbf{D}^{-1}\mathbf{R}(t), \quad (5)$$

where Δt is the time increment. We will use Eq. (5) for the analysis of the numerical dispersion of the finite element formulations with the averaged mass matrix and modified integration rule techniques. One of the main difficulties in the analytical study of numerical dispersion is the complicated non-linear structure of the equations for numerical phase velocities. Therefore, in order to simplify the dispersion analysis, we will study the residual of these equations instead of the direct calculation of the numerical phase velocities.

Propagation of harmonic plane waves u_j in an infinite elastic medium with

$$u_j(\mathbf{x}, t) = \bar{u}_j \exp(i\mathbf{k} \cdot \mathbf{x} \pm c_o t), \quad (6)$$

is used for the dispersion analysis. Here, u_j are the displacement components, \bar{u}_j are the components of the displacement amplitude vector, \mathbf{x} is the position vector, k is the wave number, \mathbf{n} is the unit normal to the wave front; $\mathbf{k} = k\mathbf{n}$ is the wave vector, c_o is the phase velocity, t is the time, $i = \sqrt{-1}$. It is known that the substitution of Eq. (6) into a system of partial differential equations for an isotropic infinite homogeneous elastic medium yields the following two solutions for the phase velocity [26]:

$$c_o = c_1 = \sqrt{\frac{\lambda + 2\mu}{\rho}} \quad \text{and} \quad c_o = c_2 = \sqrt{\frac{\mu}{\rho}}, \quad (7)$$

where c_1 and c_2 correspond to the phase velocity for the compressional and shear waves, respectively; ρ is the density; $\lambda = \frac{Ev}{(1+v)(1-2v)}$ and $\mu = \frac{E}{2(1+v)}$ are the Lame coefficients that can be also expressed in terms of Young's modulus E and Poisson's ratio v . The derivation of Eq. (7) does not include initial and boundary conditions. The phase velocities c_1 and c_2 are constant and independent of the wave vector \mathbf{k} . Therefore, an isotropic infinite homogeneous elastic medium is non-dispersive.

In the paper, we study the numerical dispersion of the linear quadrilateral finite elements on uniform meshes in the 1-D, 2-D and 3-D cases. The following procedure is used. We calculate the nodal displacements in terms of known nodal coordinates using Eq. (6) with $c_o = c$, then insert them into Eq. (5) with $\mathbf{R} = \mathbf{0}$ and estimate the corresponding wave velocities c . Because elastic waves propagate in all directions with the same velocity, then finite elements with the same dimensions along the coordinate axes will be used for wave propagation problems in the multi-dimensional case (e.g., see [1,6,10] and others). For example, it was shown in [10] that in contrast to uniform finite element meshes with the same dimensions along the coordinate axes, uniform meshes with different dimensions along the coordinate axes do not allow to reduce the order of the dispersion error for acoustic waves propagating in different directions in the 2-D case. In order to decrease the dispersion of finite element results, we consider the following two possibilities for the calculation of the mass and stiffness matrices: the mass matrix \mathbf{M} is calculated as a weighted average of the consistent \mathbf{M}^{cons} and lumped \mathbf{D} mass matrices with the weighting factor γ (similar to that used in [5,6,8])

$$\mathbf{M}(\gamma) = \mathbf{D}\gamma + \mathbf{M}^{cons}(1 - \gamma), \quad (8)$$

or the mass and stiffness matrices of each finite element are calculated with the modified integration rule (similar to those used in [10])

$$\mathbf{M}^e(\alpha_M) = \rho A \int_{-1}^1 \mathbf{N}^T(s) \mathbf{N}(s) \det(\mathbf{J}) ds \approx \rho A \sum_{m=1}^2 \mathbf{N}^T((-1)^m \alpha_M) \mathbf{N}((-1)^m \alpha_M) \det(\mathbf{J}), \quad (9)$$

$$\mathbf{K}^e(\alpha_K) = \int_{-1}^1 E \mathbf{B}^T(s) \mathbf{B}(s) \det(\mathbf{J}) ds \approx \sum_{m=1}^2 E \mathbf{B}^T((-1)^m \alpha_K) \mathbf{B}((-1)^m \alpha_K) \det(\mathbf{J}), \quad (10)$$

in the 1-D case,

$$\mathbf{M}^e(\alpha_M) = \rho b \int_{-1}^1 \int_{-1}^1 \mathbf{N}^T(s, t) \mathbf{N}(s, t) \det(\mathbf{J}) ds dt \approx \rho b \sum_{m=1}^2 \sum_{j=1}^2 \mathbf{N}^T((-1)^m \alpha_M, (-1)^j \alpha_M) \mathbf{N}((-1)^m \alpha_M, (-1)^j \alpha_M) \det(\mathbf{J}), \quad (11)$$

$$\mathbf{K}^e(\alpha_K) = \int_{-1}^1 \int_{-1}^1 \mathbf{B}^T(s, t) \bar{\mathbf{C}} \mathbf{B}(s, t) \det(\mathbf{J}) ds dt \approx \sum_{m=1}^2 \sum_{j=1}^2 \mathbf{B}^T((-1)^m \alpha_K, (-1)^j \alpha_K) \bar{\mathbf{C}} \mathbf{B}((-1)^m \alpha_K, (-1)^j \alpha_K) \det(\mathbf{J}) \quad (12)$$

in the 2-D case,

$$\begin{aligned} \mathbf{M}^e(\alpha_M) &= \rho \int_{-1}^1 \int_{-1}^1 \int_{-1}^1 \mathbf{N}^T(s, t, q) \mathbf{N}(s, t, q) \det(\mathbf{J}) ds dt dq \\ &\approx \rho \sum_{m=1}^2 \sum_{j=1}^2 \sum_{p=1}^2 \mathbf{N}^T((-1)^m \alpha_M, (-1)^j \alpha_M, (-1)^p \alpha_M) \mathbf{N}((-1)^m \alpha_M, (-1)^j \alpha_M, (-1)^p \alpha_M) \det(\mathbf{J}), \end{aligned} \quad (13)$$

$$\begin{aligned} \mathbf{K}^e(\alpha_K) &= \int_{-1}^1 \int_{-1}^1 \int_{-1}^1 \mathbf{B}^T(s, t, q) \bar{\mathbf{C}} \mathbf{B}(s, t, q) \det(\mathbf{J}) ds dt dq \\ &\approx \sum_{m=1}^2 \sum_{j=1}^2 \sum_{p=1}^2 \mathbf{B}^T((-1)^m \alpha_K, (-1)^j \alpha_K, (-1)^p \alpha_K) \bar{\mathbf{C}} \mathbf{B}((-1)^m \alpha_K, (-1)^j \alpha_K, (-1)^p \alpha_K) \det(\mathbf{J}) \end{aligned} \quad (14)$$

in the 3-D case. Here, \mathbf{N} and \mathbf{B} are the standard finite element shape and B matrices; $\bar{\mathbf{C}}$ is the matrix of elastic coefficients:

$$\bar{\mathbf{C}} = \frac{E(1-v)}{(1+v)(1-2v)} \begin{pmatrix} 1 & \frac{v}{1-v} & 0 \\ \frac{v}{1-v} & 1 & 0 \\ 0 & 0 & \frac{1-2v}{2(1-v)} \end{pmatrix}$$

in the 2-D case of plane strain and

$$\bar{\mathbf{C}} = \frac{E(1-v)}{(1+v)(1-2v)} \begin{pmatrix} 1 & \frac{v}{1-v} & \frac{v}{1-v} & 0 & 0 & 0 \\ \frac{v}{1-v} & 1 & \frac{v}{1-v} & 0 & 0 & 0 \\ \frac{v}{1-v} & \frac{v}{1-v} & 1 & 0 & 0 & 0 \\ 0 & 0 & 0 & \frac{1-2v}{2(1-v)} & 0 & 0 \\ 0 & 0 & 0 & 0 & \frac{1-2v}{2(1-v)} & 0 \\ 0 & 0 & 0 & 0 & 0 & \frac{1-2v}{2(1-v)} \end{pmatrix}$$

in the 3-D case; the diagonal terms of the lumped mass matrix \mathbf{D} (except those for the boundary nodes) for the linear elements are dx ; dx^2 ; dx^3 in the 1-D case, in the 2-D case for square elements and in the 3-D case for cubic elements, respectively; \mathbf{J} is the Jacobian matrix ($\det(\mathbf{J}) = dx/2$; $dx^2/4$; $dx^3/8$ in the 1-D case, in the 2-D case for square elements and in the 3-D case for cubic elements, respectively); dx is the length of a finite element; A is the cross sectional area in the 1-D case; b is the thickness in the 2-D case of plane strain; s, t, q are the isoparametric coordinates; α_M and α_K are the coordinates of the integration points for the mass and stiffness matrices to be determined ($2, 2 \times 2 = 4$ and $2 \times 2 \times 2 = 8$ integration points are used for linear elements in the 1-D, 2-D and 3-D cases, respectively); e.g., see [24,25] for the derivation of the finite element matrices. The integration error due to the application of the modified integration rule for the mass and stiffness matrices does not change the convergence rate of finite element solutions; see [10]. We use the dispersion analysis presented below in order to find such γ, α_M and α_K that reduce the dispersion error.

2.1. Dispersion analysis in the 1-D case

For the analysis of the numerical phase velocity of harmonic plane waves on a uniform mesh in the 1-D case, only one algebraic expression for any node should be used. It can be obtained by the substitution of the nodal displacements calculated with the help of Eq. (6) into the left-hand side of Eq. (5) where the numerical wave velocity c is used in Eq. (6) instead of c_0 . This expression \tilde{R} can be derived by the consideration of two adjacent elements with the common node (see Fig. 1(a)) and has the following form

$$\tilde{R} = \bar{R} \exp(i k(x - ct)), \quad (15)$$

where

$$\bar{R} = \frac{3(\gamma + 1)c_0^2 + ((\gamma - 1)\cos(2kdx) - 2(2\gamma + 1)\cos(kdx))c_0^2 + 6dx^2(\cos(kc\Delta t) - 1)/\Delta t^2}{3dx}, \quad (16)$$

in the case of the use of Eq. (8) and

$$\bar{R} = \frac{(3\alpha_M^2 + 1)c_0^2 + ((\alpha_M^2 - 1)\cos(2kdx) - 4\alpha_M^2 \cos(kdx))c_0^2 + 4dx^2(\cos(kc\Delta t) - 1)/\Delta t^2}{2dx}, \quad (17)$$

in the case of the use of Eq. (9) (in the 1-D case the stiffness matrix K^e is constant for linear elements and is independent of the coordinates α_K of the integration points). Here $c_0 = \sqrt{E/\rho}$ is the wave velocity in the 1-D case. Because for harmonic plane waves the right-hand side of Eq. (5) is zero, then this leads to the following algebraic equation $\tilde{R}(c) = \bar{R}(c) = 0$. From this equation we can find the numerical wave velocity c , the dispersion error $\frac{c-c_0}{c_0}$ and the parameters γ and α_M which reduce the dispersion error (for numerical solutions, the wave velocity c differs from the exact wave velocity c_0 that leads to the numerical dispersion error $\Delta c = c - c_0$). However, the same results related to the reduction in the wave velocity error can

be obtained if we expand the residual \bar{R} of Eq. (16) or Eq. (17) into the Taylor series at $c = c_0$ (e.g., see our paper [18] for implicit methods). The second approach will be used in the current paper. As can be seen from Eqs. (16) and (17), the residual \bar{R} on uniform meshes is independent of x and t , and its expansion into the Taylor series at $c = c_0$ and small dx and Δt (i.e., at $kdx \ll 1$ and $kc_0\Delta t \ll 1$) yields

$$\bar{R}(c = c_0) = \frac{1}{12} c_0^2 dx^3 (\bar{\tau}^2 + 2\gamma - 3) k^4 + \frac{1}{360} (11 - 10\gamma - \bar{\tau}^4) c_0^2 dx^5 k^6 + O(dx^6), \quad (18)$$

for Eq. (16)

$$\bar{R}(c = c_0) = \frac{1}{12} c_0^2 dx^3 (3\alpha_M^2 + \bar{\tau}^2 - 4) k^4 + \frac{1}{360} (16 - 15\alpha_M^2 - \bar{\tau}^4) c_0^2 dx^5 k^6 + O(dx^6), \quad (19)$$

for Eq. (17) where $\bar{\tau} = \frac{c_0 \Delta t}{dx}$ is the Courant number.

Due to the difference between the exact and numerical wave velocities for harmonic plane waves, the residual \bar{R} in Eqs. (18) and (19) is non-zero at $c = c_0$. The smaller residual means the smaller difference between the exact and numerical wave velocities. For small dx , the order of the leading term for the residual \bar{R} (the order of accuracy) increases at $\gamma = \gamma^{opt} = \frac{3-\bar{\tau}^2}{2}$ (see the first term in Eq. (18)) and at $\alpha_M = \alpha_M^{opt} = \sqrt{\frac{4-\bar{\tau}^2}{3}}$ (see the first term in Eq. (19)). We should mention that at $\bar{\tau} \approx 0$ (for very small time increments), the optimal value of $\gamma^{opt} = \frac{3}{2}$ coincides with the results obtained in [5] for the 1-D case. However, the size of time increments significantly affects γ^{opt} . For example, the stability limit for the time integration of Eq. (5) on uniform meshes with linear elements equals $\Delta t^{st} = \frac{dx}{c_0}$ or $\bar{\tau} = 1$. In this case, $\gamma^{opt} = 1$ and $\mathbf{M} = \mathbf{D}$ (see Eq. (8)); i.e., for this particular case, Eq. (5) reduces to the standard finite element formulation with the lumped mass matrix (it is known that in the 1-D case, the standard linear finite elements and the explicit central difference method yield the exact solution to the 1-D impact problem at $\bar{\tau} = 1$; e.g., see [24]). It can be also seen that at $\gamma^{opt} = \frac{3-\bar{\tau}^2}{2}$, the first term in Eq. (18) is zero, the second term in Eq. (18) equals $\frac{1}{360}(\bar{\tau}^2 - 1)(\bar{\tau}^2 - 4)c_0^2 dx^5 k^6$ and is zero at $\bar{\tau} = 1$ and increases with the decrease in $\bar{\tau}$ (for $\bar{\tau} < 1$). This means that for linear elements with the averaged mass matrix and 1-D uniform meshes, the dispersion error increases with the decrease in the size of time increments Δt for the time increments smaller than the stability limit.

At $\gamma = (3\alpha_M^2 - 1)/2$, Eqs. (16) and (17) are equivalent and yield the same relationships between the exact c_0 and numerical c wave velocities (with the optimal value of $\alpha_M^{opt} = \sqrt{\frac{4-\bar{\tau}^2}{3}}$ as in [10]). The mass matrices calculated with the use of Eqs. (8) and (9) are also equivalent at $\gamma = (3\alpha_M^2 - 1)/2$ (e.g., $\gamma = 1$ and $\alpha_M = \pm 1$ correspond to the lumped matrix). This means that the modified integration rule and the averaged mass matrix are completely equivalent techniques in the 1-D case.

2.2. Dispersion analysis in the 2-D case (plane strain)

For the analysis of the numerical phase velocity of the harmonic plane waves on a uniform mesh in the 2-D case (plane strain), only two algebraic equations (for the x and y directions) for any node should be used. They can be obtained by the substitution of the nodal displacements (calculated with the help of Eq. (6)) into Eq. (5). These two homogeneous equations, which are linear with respect to two unknown amplitudes \bar{u}_1 and \bar{u}_2 , can be determined by the consideration of four adjacent elements with the common node; see Fig. 1(b). For non-zero amplitudes of the displacements \bar{u}_1 and \bar{u}_2 , the determinant R of the system of algebraic equations has to be zero. Due to lengthy expression for the determinant R , we present it only for small dx (dx is the length of a square finite element)

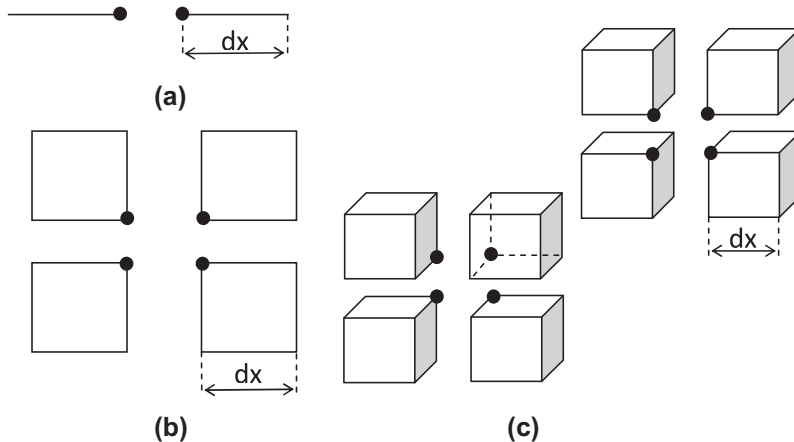


Fig. 1. Adjacent quadrilateral finite elements used for the derivation of the dispersion equation for the common node in the 1-D (a), 2-D (b) and 3-D (c) cases.

$$R = (a_4 dx^4 + a_6 dx^6 + O(dx^8)) \exp(2ik(x \cos(\Theta) + y \sin(\Theta) - ct)), \quad (20)$$

where the expressions for coefficients a_4 and a_6 are given below for different techniques.

2.2.1. The modified integration rule

In the case of the calculation of the mass and stiffness matrices with the help of Eqs. (11) and (12), the coefficients a_4 and a_6 can be found as follows:

$$\begin{aligned} a_4 &= \frac{1}{2v-1} k^4 \left(c^2 - \frac{\mu}{\rho} \right) \left(c^2(2v-1) - 2 \frac{\mu}{\rho}(v-1) \right), \\ a_6 &= \frac{k^6}{96(c_2 - 2c_1)^2} (16\tau^2(1-2v)^2 c^6 - 8(\frac{\mu}{\rho})\tau^2(2v(4v-5)+3)c^4 + 6(4\alpha_M^2 + \alpha_K^2 - 6)\alpha_2^2(\frac{\mu}{\rho})(2v(4v-5)+3)c^2 \\ &\quad - 3\alpha_2^2(\frac{\mu}{\rho})^2(32(v-1)(2v-1)\alpha_M^2 + \alpha_K^2(3-4v)^2 - 48(v-1)(2v-1)) + \alpha_2^2(\frac{\mu}{\rho})(\frac{\mu}{\rho})(3\alpha_K^2(3-4v)^2 \\ &\quad - 16(v-1)(2v-1) - 2(3\alpha_K^2 - 2)c^2(2v(4v-5)+3)) \cos(4\Theta)). \end{aligned} \quad (21)$$

Here $\tau = \frac{c_2 \Delta t}{dx}$ is the Courant number, the components of the unit vector \mathbf{n} in Eq. (6) are represented as $n_1 = \cos(\Theta)$ and $n_2 = \sin(\Theta)$. The difference between the numerical and exact wave velocities for plane waves can be estimated by means of the leading term of the residual R in Eq. (20) at small dx for $c = c_1$ and for $c = c_2$ (see the explanations for the 1-D case). At $c = c_1$ and at $c = c_2$, coefficient a_4 is zero ($a_4 = 0$), and coefficient a_6 has the following forms:

$$a_6(c = c_1) = \frac{k^6(\frac{\mu}{\rho})^2}{96(2v-1)^3} \{ [-48(v-1)(2v-1)\alpha_M^2 - 8(4(v-1)\tau^2 - 18v+9)(v-1) - 3\alpha_K^2(2v(4v-5)+3)] \\ + [(2v-1)(3(4v-3)\alpha_K^2 - 8v+8)] \cos(4\Theta) \} \quad (22)$$

and

$$a_6(c = c_2) = -\frac{k^6(\frac{\mu}{\rho})^2}{96(1-2v)^2} \{ [24(2v-1)\alpha_M^2 + 4(2\tau^2 - 9)(2v-1) + 3\alpha_K^2(4v-3)] + [(9-12v)\alpha_K^2 + 8v-4] \cos(4\Theta) \}. \quad (23)$$

Assuming that the expressions in two square brackets of Eq. (22) (or Eq. (23)) are zeros, from these two algebraic equations we can find such α_K and α_M at which $a_6(c = c_1) = 0$ (or $a_6(c = c_2) = 0$). Unfortunately, these solutions for α_K and α_M are different for Eqs. (22) and (23). This means that we can only find such α_K and α_M at which a_6 is zero for one of Eqs. (22) and (23); i.e., at $\alpha_M = \sqrt{\frac{4-\tau^2}{3}}$ and $\alpha_K = \sqrt{\frac{4(2v-1)}{3(4v-3)}}$ Eqs. (22) and (23) reduce to

$$\begin{aligned} a_6 \left(c = c_1, \alpha_M = \sqrt{\frac{4-\tau^2}{3}}, \alpha_K = \sqrt{\frac{4(2v-1)}{3(4v-3)}} \right) &= \frac{k^6(\frac{\mu}{\rho})^2}{24(2v-1)^3} (4(v-1)\tau^2 - 2v + (2v-1) \cos(4\Theta) + 1), \\ a_6 \left(c = c_2, \alpha_M = \sqrt{\frac{4-\tau^2}{3}}, \alpha_K = \sqrt{\frac{4(2v-1)}{3(4v-3)}} \right) &= 0, \end{aligned} \quad (24)$$

or at $\alpha_M = \sqrt{\frac{4-(\tau c_1/c_2)^2}{3}}$ and $\alpha_K = \sqrt{\frac{8(1v-1)}{3(4v-3)}}$ Eqs. (22) and (23) reduce to

$$\begin{aligned} a_6 \left(c = c_1, \alpha_M = \sqrt{\frac{4-(\tau c_1/c_2)^2}{3}}, \alpha_K = \sqrt{\frac{8(1v-1)}{3(4v-3)}} \right) &= 0, \\ a_6 \left(c = c_2, \alpha_M = \sqrt{\frac{4-(\tau c_1/c_2)^2}{3}}, \alpha_K = \sqrt{\frac{8(1v-1)}{3(4v-3)}} \right) &= \frac{k^6(\frac{\mu}{\rho})^2}{24(1-2v)^2} (2\tau^2 + \cos(4\Theta) - 1). \end{aligned} \quad (25)$$

As will be shown later (see Eq. (A.3) below), the plane waves with velocity $c = c_2$ yield a greater error in numerical solutions than the plane waves with velocity $c = c_1$. Therefore, the optimal choice for the selection of α_M and α_K corresponds to $\alpha_M = \sqrt{\frac{4-\tau^2}{3}}$ and $\alpha_K = \sqrt{\frac{4(2v-1)}{3(4v-3)}}$ used in Eq. (24). In this case (see Eq. (24)), coefficient $a_6 = 0$ is zero for the shear plane waves ($c = c_2$) propagating in all directions at any τ and for the compressional plane waves ($c = c_1$) propagating along the x_1 ($\Theta = 0$) or x_2 ($\Theta = \pi/2$) axis at $\tau = 0$ (for very small time increments).

Similar results can be found if the mass matrix is calculated according to Eq. (8) and the stiffness matrix is calculated according to Eq. (12). In this case, coefficient a_4 is the same as in Eq. (21) and coefficient a_6 is calculated as follows:

$$a_6 = \frac{k^6}{96\left(\frac{\mu}{\rho}\right)(1-2v)^2} (16\tau^2(1-2v)^2c^6 - 8\left(\frac{\mu}{\rho}\right)\tau^2(2v(4v-5)+3)c^4 + 2(3\alpha_K^2+8\gamma-14)\left(\frac{\mu}{\rho}\right)^2(2v(4v-5)+3)c^2 \\ + \left(\frac{\mu}{\rho}\right)^3(-3\alpha_K^2(3-4v)^2 - 16(4\gamma-7)(v-1)(2v-1)) + \left(\frac{\mu}{\rho}\right)^2\left(\left(\frac{\mu}{\rho}\right)(3\alpha_K^2(3-4v)^2 - 16(v-1)(2v-1))\right. \\ \left.- 2(3\alpha_K^2-2)c^2(2v(4v-5)+3)\right)\cos(4\Theta)). \quad (26)$$

Then, similar to the use of the modified integration rule for the mass matrix in Eqs. (24) and (25), coefficient a_6 is zero for one of the plane waves at $\gamma = \frac{3-\tau^2}{2}$ and $\alpha_K = \sqrt{\frac{4(2v-1)}{3(4v-3)}}$

$$a_6 \left(c = c_1, \gamma = \frac{3-\tau^2}{2}, \alpha_K = \sqrt{\frac{4(2v-1)}{3(4v-3)}} \right) = a_6 \left(c = c_1, \alpha_M = \sqrt{\frac{4-\tau^2}{3}}, \alpha_K = \sqrt{\frac{4(2v-1)}{3(4v-3)}} \right), \\ a_6 \left(c = c_2, \gamma = \frac{3-\tau^2}{2}, \alpha_K = \sqrt{\frac{4(2v-1)}{3(4v-3)}} \right) = 0, \quad (27)$$

or at $\gamma = \frac{3-\tau^2}{2}$ and $\alpha_K = \sqrt{\frac{8(1v-1)}{3(4v-3)}}$

$$a_6 \left(c = c_1, \gamma = \frac{3-(\tau c_1/c_2)^2}{2}, \alpha_K = \sqrt{\frac{8(1v-1)}{3(4v-3)}} \right) = 0, \\ a_6 \left(c = c_2, \gamma = \frac{3-(\tau c_1/c_2)^2}{2}, \alpha_K = \sqrt{\frac{8(1v-1)}{3(4v-3)}} \right) = a_6 \left(c = c_2, \alpha_M = \sqrt{\frac{4-(\tau c_1/c_2)^2}{3}}, \alpha_K = \sqrt{\frac{8(1v-1)}{3(4v-3)}} \right). \quad (28)$$

However, we should mention that in contrast to the 1-D case, the mass matrices calculated by the use of Eq. (11) at $\alpha_M = \sqrt{\frac{4-\tau^2}{3}}$ and by the use of Eq. (8) at $\gamma = \frac{3-\tau^2}{2}$ are different in the 2-D case; e.g., at $\tau = 0$ these matrices are:

$$\mathbf{M} \left(\alpha_M = \sqrt{\frac{4}{3}} \right) = \begin{pmatrix} 49 & 0 & -7 & 0 & 1 & 0 & -7 & 0 \\ 0 & 49 & 0 & -7 & 0 & 1 & 0 & -7 \\ -7 & 0 & 49 & 0 & -7 & 0 & 1 & 0 \\ 0 & -7 & 0 & 49 & 0 & -7 & 0 & 1 \\ 1 & 0 & -7 & 0 & 49 & 0 & -7 & 0 \\ 0 & 1 & 0 & -7 & 0 & 49 & 0 & -7 \\ -7 & 0 & 1 & 0 & -7 & 0 & 49 & 0 \\ 0 & -7 & 0 & 1 & 0 & -7 & 0 & 49 \end{pmatrix} \frac{\rho dx^2}{144} \quad (29)$$

and

$$\mathbf{M} \left(\gamma = \frac{3}{2} \right) = \begin{pmatrix} 46 & 0 & -4 & 0 & -2 & 0 & -4 & 0 \\ 0 & 46 & 0 & -4 & 0 & -2 & 0 & -4 \\ -4 & 0 & 46 & 0 & -4 & 0 & -2 & 0 \\ 0 & -4 & 0 & 46 & 0 & -4 & 0 & -2 \\ -2 & 0 & -4 & 0 & 46 & 0 & -4 & 0 \\ 0 & -2 & 0 & -4 & 0 & 46 & 0 & -4 \\ -4 & 0 & -2 & 0 & -4 & 0 & 46 & 0 \\ 0 & -4 & 0 & -2 & 0 & -4 & 0 & 46 \end{pmatrix} \frac{\rho dx^2}{144}. \quad (30)$$

Remark. The selection of time increments Δt (or τ) in the 2-D case differs from that in the 1-D case described in Section 2.1. Because we can zero the coefficient a_6 in the expression for the dispersion error, Eqs. (22) and (22), for one plane wave with $c = c_1$ or $c = c_2$, then for another plane wave we can only minimize non-zero coefficient a_6 by the selection of τ (or Δt). Let us consider non-zero coefficient a_6 in the first formula of Eq. (24). If we find τ from the condition that

$a_6 \left(c = c_1, \alpha_M = \sqrt{\frac{4-\tau^2}{3}}, \alpha_K = \sqrt{\frac{4(2v-1)}{3(4v-3)}} \right) = 0$ then we will get $\tau^2 = \frac{(1-2v)\sin^2(2\Theta)}{2(1-v)}$. This means that τ is different for different Θ

and $a_6 \left(c = c_1, \alpha_M = \sqrt{\frac{4-\tau^2}{3}}, \alpha_K = \sqrt{\frac{4(2v-1)}{3(4v-3)}} \right)$ cannot be zero for all Θ for the compressional plane wave with $c = c_1$. As we mentioned before, in order to zero a_6 for the compressional plane wave propagating along the x_1 ($\Theta = 0$) or x_2 ($\Theta = \pi/2$) we should use very small time increments Δt at which τ is close to zero. In the case of very small time increments ($\tau \approx 0$), the first coefficient a_6 in Eq. (24) can be simplified as follows:

$$a_6 \left(c = c_1, \alpha_M = \sqrt{\frac{4}{3}}, \alpha_K = \sqrt{\frac{4(2v-1)}{3(4v-3)}}, \tau = 0 \right) = -\frac{k^6 \left(\frac{\mu}{\rho}\right)^2 \sin^2(2\Theta)}{12(2v-1)^3}. \quad (31)$$

We will also analyze the selection of optimal time increments using numerical experiments (see Section 3 below).

Remark. It is interesting to note that small time increments are also required for the dispersion-reduction technique used in our paper [18] with the implicit trapezoidal rule. It seems that for any time-integration method, the error in time does not compensate the error in space in the multidimensional case. Therefore, small time increments can be recommended for the reduction of the error in time.

2.2.2. The averaged mass matrix

For the averaged mass matrix, coefficient a_4 is the same as that in Eq. (21) and coefficient a_6 is given by Eq. (26). At $\gamma = \frac{3-\tau^2}{2}$ (as in Eq. (27)) and the standard stiffness matrix (this corresponds to the use of Eq. (12) with $\alpha_K = \sqrt{\frac{1}{3}}$), it follows from Eq. (26) that in the general case, coefficient a_6 is non-zero for both plane waves at $c = c_1$ and at $c = c_2$ (coefficient a_4 is zero); i.e.,

$$\begin{aligned} a_6 \left(c = c_1, \gamma = \frac{3-\tau^2}{2}, \alpha_K = \sqrt{\frac{1}{3}} \right) &= \frac{k^6 \left(\frac{\mu}{\rho}\right)^2}{96(2v-1)^3} (16(v-1)\tau^2 + 2v(4v-7) + (2(7-4v)v-5) \cos(4\Theta) + 5), \\ a_6 \left(c = c_2, \gamma = \frac{3-\tau^2}{2}, \alpha_K = \sqrt{\frac{1}{3}} \right) &= \frac{k^6 \left(\frac{\mu}{\rho}\right)^2 (-1+4v) \sin^2(2\Theta)}{48(1-2v)^2}. \end{aligned} \quad (32)$$

However, coefficient a_6 is zero for the plane wave propagating along the x_1 ($\Theta = 0$) or x_2 ($\Theta = \pi/2$) axis at any τ for the shear wave ($c = c_2$) and at $\tau = 0$ (for very small time increments) for the compressional wave ($c = c_1$); see Eq. (32). In the case of very small time increments ($\tau = 0$), the first coefficient a_6 in Eq. (32) can be simplified as follows:

$$a_6 \left(c = c_1, \gamma = \frac{3}{2}, \alpha_K = \sqrt{\frac{1}{3}}, \tau = 0 \right) = \frac{k^6 \left(\frac{\mu}{\rho}\right)^2 (-5+4v) \sin^2(2\Theta)}{48(1-2v)^2}. \quad (33)$$

We will also analyze the selection of optimal time increments using numerical experiments (see Section 3 below).

2.2.3. Existing approaches

For the existing approaches with the lumped ($\gamma = 1$) mass matrix and the standard stiffness matrix ($\alpha_K = \sqrt{\frac{1}{3}}$), coefficient a_6 is non-zero and has the following values (coefficient a_4 is zero at $c = c_1$ and at $c = c_2$):

$$\begin{aligned} a_6 \left(c = c_1, \gamma = 1, \alpha_K = \sqrt{\frac{1}{3}} \right) &= \frac{k^6 \left(\frac{\mu}{\rho}\right)^2}{96(2v-1)^3} (-32\tau^2(v-1)^2 + 40v^2 - 62v + (2(7-4v)v-5) \cos(4\Theta) + 21), \\ a_6 \left(c = c_2, \gamma = 1, \alpha_K = \sqrt{\frac{1}{3}} \right) &= \frac{k^6 \left(\frac{\mu}{\rho}\right)^2}{96(1-2v)^2} (8(2v-1)\tau^2 - 20v + (4v-1) \cos(4\Theta) + 9). \end{aligned} \quad (34)$$

Using these results, we can estimate the effect of a time increment Δt (or τ) on the dispersion error for the standard central difference with the lumped mass matrix in the 2-D case. For example, as our numerical results and the formula (A.3) (see also our paper [22]) show, the range of spurious oscillations and the accuracy of numerical results are defined by the harmonic waves propagating with the velocity c_2 or by the coefficient $a_6(c = c_2, \gamma = 1, \alpha_K = \sqrt{\frac{1}{3}})$ in Eq. (34). This coefficient is zero at $\tau^2 = \tau_0^2 = \frac{20v+(1-4v)\cos(4\Theta)-9}{16v-8}$. However, admissible τ^2 may vary between $0 \leq \tau^2 \leq \tau_{max}^2$ where $\tau_{max} = \frac{c_2 \Delta t^{st}}{dx}$. The stability limit Δt^{st} in the 2-D case for the plane strain state equals $\Delta t^{st} = \frac{dx}{c_1}$; e.g., see [1]. This means that $\tau_{max} = \frac{c_2}{c_1} = \sqrt{1 - \frac{1}{2(1-v)}}$. The comparison of these expressions for τ_0^2 and τ_{max}^2 shows that at $0 \leq v \leq \frac{9-\sqrt{33}}{8} = 0.40693$, we have $\tau_0^2 \geq \tau_{max}^2$ at any Θ . This means that coefficient $a_6(c = c_2, \gamma = 1, \alpha_K = \sqrt{\frac{1}{3}})$ in Eq. (34) has the minimum value at $\tau = \tau_{max}$ among all admissible τ and $0 \leq v \leq 0.40693$. For $0.40693 < v \leq 0.5$ and some angles Θ , the coefficient $a_6(c = c_2, \gamma = 1, \alpha_K = \sqrt{\frac{1}{3}})$ in Eq. (34) has the minimum value for $\tau < \tau_{max}$ (or for $\Delta t < \Delta t^{st}$). However, even at $\tau = \tau_{max}$ (or $\Delta t = \Delta t^{st}$), the difference between coefficient $a_6(c = c_2, \gamma = 1, \alpha_K = \sqrt{\frac{1}{3}})$ at $\Delta t = \Delta t^{st}$ ($\tau = \tau_{max}$) and $\Delta t = 0$ ($\tau = 0$) is not very big. For example, for different angles Θ , the ratio $\frac{a_6(\Delta t = \Delta t^{st})}{a_6(\Delta t = 0)}$ for coefficient $a_6(c = c_2, \gamma = 1, \alpha_K = \sqrt{\frac{1}{3}})$ in Eq. (34) varies between $0.55 \div 0.63$ at $v = 0.1, 0.67 \div 0.72$ at $v = 0.3, 0.35 \div 0.83$ at $v = 0.4$. These results are very different from the 1-D case for which the dispersion error and the corresponding coefficients in the Taylor series for the dispersion error are zero at $\Delta t = \Delta t^{st}$ (see the discussion after Eq. (19)). For convenience, below we present the coefficients a_6 in Eq. (34) at $\tau = 0$:

$$\begin{aligned} a_6 \left(c = c_1, \gamma = 1, \alpha_M = \sqrt{\frac{1}{3}}, \tau = 0 \right) &= -\frac{k^6 \left(\frac{\mu}{\rho}\right)^2}{96(2v-1)^2} (21 - 20v + (4v-5) \cos(4\Theta)), \\ a_6 \left(c = c_2, \gamma = 1, \alpha_K = \sqrt{\frac{1}{3}}, \tau = 0 \right) &= \frac{k^6 \left(\frac{\mu}{\rho}\right)^2}{96(1-2v)^2} (9 - 20v + (4v-1) \cos(4\Theta)). \end{aligned} \quad (35)$$

2.3. Dispersion analysis in the 3-D case

For the analysis of the numerical phase velocity of the plane waves on a uniform mesh in the 3-D case, only three algebraic equations (for the x, y and z directions) for any node should be used. They can be obtained by the substitution of the nodal displacements (calculated with the help of Eq. (6)) into Eq. (5). These three homogeneous equations, which are linear with respect to three unknown amplitudes \bar{u}_1, \bar{u}_2 and \bar{u}_3 , can be determined by the consideration of eight adjacent elements with the common node; see Fig. 1(c). For non-zero solutions for the displacements \bar{u}_1, \bar{u}_2 and \bar{u}_3 , the determinant R of the system of algebraic equations has to be zero. Due to lengthy expression for the determinant R , we present it only for small dx (dx is the length of a cubic finite element):

$$\begin{aligned} R &= (a_6 dx^6 + a_8 dx^8 + a_{10} dx^{10} + O(dx^{11})) \\ &\exp(3ik(x \cos(\Theta) + y \sin(\Theta) \cos(\Psi) + z \sin(\Theta) \sin(\Psi) - ct)), \end{aligned} \quad (36)$$

with

$$a_6 = \frac{1}{2v-1} k^6 \left(c^2 - \frac{\mu}{\rho} \right)^2 \left(c^2(2v-1) - 2 \frac{\mu}{\rho} (v-1) \right). \quad (37)$$

Here the components of the unit vector \mathbf{n} in Eq. (6) are represented in terms of two angles Θ and Ψ as $n_1 = \cos(\Theta), n_2 = \sin(\Theta) \cos(\Psi)$ and $n_3 = \sin(\Theta) \sin(\Psi)$. At $c = c_1$ and at $c = c_2$, coefficient a_6 is zero (see Eq. (37)). At $c = c_2$, coefficient a_8 is zero at any α_M and α_K (in the 3-D case there are three roots of the determinant for the phase velocity c , two of them are the same and equal $c = c_2$). In the 3-D case, the increase in accuracy for the calculation of the phase velocity corresponds to the decrease in the absolute value of coefficient a_8 at $c = c_1$ and to the decrease in the absolute value of coefficient a_{10} at $c = c_2$.

2.3.1. The modified integration rule

Below we present coefficients a_8 and a_{10} at the optimal values of $\alpha_M = \sqrt{\frac{4-\tau^2}{3}}$ and $\alpha_K = \sqrt{\frac{4(2v-1)}{3(4v-3)}}$ determined above in the 2-D case:

$$\begin{aligned} a_8 \left(c = c_1, \alpha_M = \sqrt{\frac{4-\tau^2}{3}}, \alpha_K = \sqrt{\frac{4(2v-1)}{3(4v-3)}} \right) &= \frac{k^8 \left(\frac{\mu}{\rho}\right)^3}{768(1-2v)^4(4v-3)} (-48 \cos(4\Psi) \sin^4(\Theta) - 128\tau^2(v-1)(4v-3) \\ &+ 2(2v-1)(82v-63) - 78 \cos(4\Theta) - 3 \cos(6\Theta) \\ &+ \cos(2\Theta)(48(1-2v)^2 \cos(4\Psi) \sin^4(\Theta) - 116v^2 + 148v - 45) \\ &+ 4v(-16(v-2) \cos(4\Psi) \sin^4(\Theta)(64-50v) \cos(4\Theta) - 3(v-1) \cos(6\Theta))), \\ a_{10} \left(c = c_2, \alpha_M = \sqrt{\frac{4-\tau^2}{3}}, \alpha_K = \sqrt{\frac{4(2v-1)}{3(4v-3)}} \right) &= \frac{k^{10} \left(\frac{\mu}{\rho}\right)^3 \sin^4(\Theta) \sin^2(2\Theta) \sin^2(2\Psi)}{576(3-4v)^2(2v-1)} \\ &\times (-2 \cos(4\Psi) \sin^2(\Theta) + 7 \cos(2\Theta) + 9). \end{aligned} \quad (38)$$

Similar results can be found if the mass matrix is calculated according to Eq. (8) (the averaged mass matrix) and the stiffness matrix is calculated according to Eq. (14) (the modified integration rule). In this case

$$\begin{aligned} a_8(c = c_1, \gamma = \frac{3-\tau^2}{2}, \alpha_K = \sqrt{\frac{4(2v-1)}{3(4v-3)}}) &= a_8(c = c_1, \alpha_M = \sqrt{\frac{4-\tau^2}{3}}, \alpha_K = \sqrt{\frac{4(2v-1)}{3(4v-3)}}, \\ a_{10}(c = c_2, \gamma = \frac{3-\tau^2}{2}, \alpha_K = \sqrt{\frac{4(2v-1)}{3(4v-3)}}) &= a_{10}(c = c_2, \alpha_M = \sqrt{\frac{4-\tau^2}{3}}, \alpha_K = \sqrt{\frac{4(2v-1)}{3(4v-3)}}, \end{aligned} \quad (39)$$

i.e., coefficients a_8 and a_{10} are the same as in Eq. (38). However, the mass matrices calculated by the use of Eq. (8) at $\gamma = \frac{3-\tau^2}{2}$ or by the use of Eq. (13) at $\alpha_M = \sqrt{\frac{4-\tau^2}{3}}$ are different (similar to the considered 2-D case).

As can be seen from Eq. (38), in the 3-D case (in contrast to the 1-D and 2-D cases) the modified integration rule for the mass and stiffness matrices does not increase the order of accuracy of the phase velocity of the shear plane waves for all possible directions of the unit vector \mathbf{n} . However, for the harmonic shear waves ($c = c_2$) propagating in the planes x_1x_2 ($\Psi = 0$), x_1x_3 ($\Psi = \pi/2$) or x_2x_3 ($\Theta = \pi/2$), coefficient a_{10} is zero $a_{10} = 0$ at any τ (see Eq. (38)); i.e., the order of accuracy in the calculation of the phase velocity of the harmonic shear waves in these directions is increased at $\alpha_M = \sqrt{\frac{4-\tau^2}{3}}$ (or $\gamma = \frac{3-\tau^2}{2}$) and $\alpha_K = \sqrt{\frac{4(2v-1)}{3(4v-3)}}$. For the compressional harmonic plane waves ($c = c_1$) propagating in the directions of the x_1 ($\Theta = 0$), x_2 ($\Theta = \pi/2$ and $\Psi = 0$) or x_3 ($\Theta = \pi/2$ and $\Psi = \pi/2$) axis, the coefficient $a_8 = 0$ at $\tau = 0$ (or very small time increments); i.e., the order of accuracy in the calculation of the phase velocity of the harmonic compressional waves in these directions is increased at $\alpha_M = \sqrt{\frac{4}{3}}$ (or $\gamma = \frac{3}{2}$), $\alpha_K = \sqrt{\frac{4(2v-1)}{3(4v-3)}}$ and $\tau = 0$ (i.e., at very small time increments $\Delta t \approx 0$). In the case of very small time increments ($\tau = 0$), coefficient a_8 in Eq. (38) can be simplified as follows (coefficient a_{10} in Eq. (38) is independent of τ):

$$\begin{aligned} a_8(c = c_1, \alpha_M = \sqrt{\frac{4}{3}}, \alpha_K = \sqrt{\frac{4(2v-1)}{3(4v-3)}}, \tau = 0) \\ = \frac{k^8(\frac{\mu}{\rho})^3 \sin^2(\Theta)}{192(1-2v)^3(4v-3)} (4(-2v + (6v-3)\cos(2\Theta) + 3)\cos(4\Psi)\sin^2(\Theta) + 138v + 112v\cos(2\Theta) - 84 \\ \times \cos(2\Theta) + 6v\cos(4\Theta) - 3\cos(4\Theta) - 105). \end{aligned} \quad (40)$$

2.3.2. The averaged mass matrix

Below we present coefficients a_8 and a_{10} for the averaged mass matrix with the optimal value of $\gamma = \frac{3-\tau^2}{2}$ and the standard stiffness matrix ($\alpha_K = \sqrt{\frac{1}{3}}$):

$$\begin{aligned} a_8 \left(c = c_1, \gamma = \frac{3 - \tau^2}{2}, \alpha_K = \sqrt{\frac{1}{3}} \right) = \frac{k^8(\frac{\mu}{\rho})^3}{3072(1-2v)^4} (-16(2v-1)(8v-7)\cos(4\Psi)\sin^4(\Theta) + 352v^2 + 512\tau^2(v-1) \\ - 604v - 2(2v-1)(56v-67)\cos(4\Theta) + 6v\cos(6\Theta) - 3\cos(6\Theta) - (2v-1) \\ \times \cos(2\Theta)(48\cos(4\Psi)\sin^4(\Theta) + 64v - 77) + 214), \\ a_{10} \left(c = c_2, \gamma = \frac{3 - \tau^2}{2}, \alpha_K = \sqrt{\frac{1}{3}} \right) = \frac{k^{10}(\frac{\mu}{\rho})^3 \sin^4(\Theta)}{589824(2v-1)^3} [16(4v(8v-9) + (7-12v)\cos(2\Theta) + 11)\cos(8\Psi) \\ \times \sin^4(\Theta) - 16(12v(48v-49) + 8(56v^2 - 66v + 21)\cos(2\Theta) + (21 \\ - 36v)\cos(4\Theta) + 163)\cos(4\Psi)\sin^2(\Theta) + 27200v^2 - 20856v + 32000v^2 \\ \times \cos(2\Theta) - 24156v\cos(2\Theta) + 4091\cos(2\Theta) + 6336v^2\cos(4\Theta) \\ - 4296v\cos(4\Theta) + 526\cos(4\Theta) + 156v\cos(6\Theta) - 91\cos(6\Theta) + 3666]. \end{aligned} \quad (41)$$

Similar to the 2-D case, for the averaged mass matrix the order of accuracy in the calculation of the phase velocity of the plane waves propagating in the directions of the x_1 ($\Theta = 0$), x_2 ($\Theta = \pi/2$ and $\Psi = 0$) or x_3 ($\Theta = \pi/2$ and $\Psi = \pi/2$) axis is increased for the shear plane waves at any τ and for the compressional plane waves at $\tau = 0$ (for very small time increments $\Delta t \approx 0$). In these cases, coefficients a_8 and a_{10} are zero; see Eq. (41). In the case of very small time increments ($\tau = 0$), coefficient a_8 in Eq. (41) can be simplified as follows (coefficient a_{10} in Eq. (41) is independent of τ):

$$\begin{aligned} a_8 \left(c = c_1, \alpha_M = \sqrt{\frac{4}{3}}, \alpha_K = \sqrt{\frac{4(2v-1)}{3(4v-3)}}, \tau = 0 \right) = \frac{k^8(\frac{\mu}{\rho})^3 \sin^2(\Theta)}{768(2v-1)^3} (-4(8v-7)\cos(4\Psi)\sin^2(\Theta) - 3(-48v \\ + \cos(4\Theta) + 59) + 4\cos(2\Theta)(-3\cos(4\Psi)\sin^2(\Theta) + 28v - 35)). \end{aligned} \quad (42)$$

3. Numerical modeling

The new finite element techniques with reduced dispersion are implemented into the finite element code FEAP [27]. Below they are applied to 1-D, 2-D and 3-D impact linear elastodynamics problems for which all low and high frequencies are excited. Due to spurious high-frequency oscillations, these problems cannot be accurately solved by existing time-integration methods based on the introduction of artificial viscosity (or numerical dissipation) at each time increment, especially in the case of long-term integration. Therefore, the two-stage time integration technique developed in our previous papers

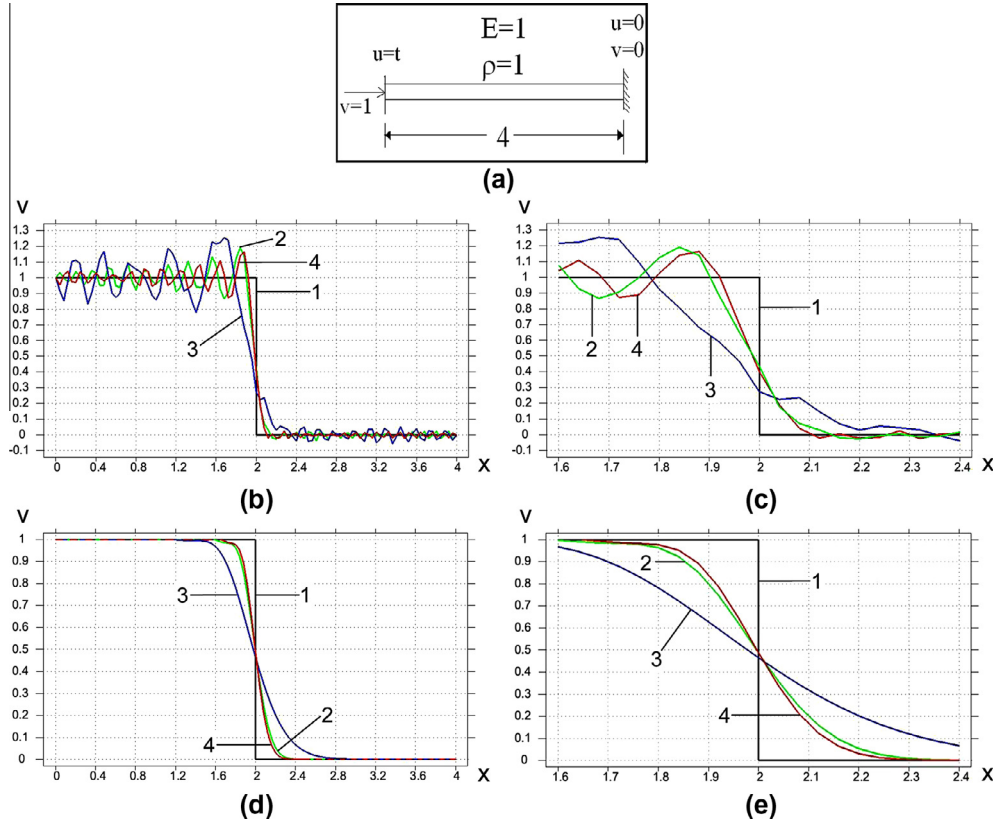


Fig. 2. Impact of an elastic bar of length $L = 4$ against a rigid wall (a). The velocity distribution along the bar at observation time $T = 18$ after basic computations with small time increments $\Delta t = \Delta t^{\text{st}}/20 = 0.002$ (b, c) and after the filtering stage (d, e). Curves 1 correspond to the analytical solution. Curves 2 and 3 correspond to the numerical solutions with the averaged ($\gamma = \frac{3-t^2}{2}$) and lumped mass matrices on a uniform mesh with 100 linear 2-node finite elements. Curves 4 correspond to the numerical solutions from our paper [22]) for the averaged mass matrix ($\gamma = 0.5$) and the implicit time-integration method on a uniform mesh with 100 linear 2-node finite elements. (c) and (e) show the zoomed graphs (b) and (d) in the range $1.6 < x < 2.4$.

[20–22] (see also the Appendix) is used with the stage of basic computations and the filtering stage. The filtering stage of this technique includes the TCG method with $N = 10$ time increments (5 positive plus 5 negative time increments) the size of which is calculated according to Eqs. (A.1)–(A.3) (see [20–22] and the Appendix below). We also compare the numerical results obtained below with those obtained in our previous paper [18] using the implicit trapezoidal rule with very small time increments at basic computations.

3.1. 1-D impact of an elastic bar against a rigid wall

First, the impact of an elastic bar of the length $L = 4$ against a rigid wall is considered in the 1-D case (see Fig. 2(a)). Young's modulus is chosen to be $E = 1$ and the density to be $\rho = 1$. The following boundary conditions are applied: the displacement $u(0, t) = t$ (which corresponds to the velocity $v(0, t) = v_0 = 1$) and $u(4, t) = 0$ (which corresponds to the velocity $v(4, t) = 0$). Initial displacements and velocities are zero; i.e., $u(x, 0) = v(x, 0) = 0$. The analytical solution to this problem for $0 < t < 4$ includes the continuous variation of displacements $u_a(x, t) = t - x$ for $t \geq x$ and $u_a(x, t) = 0$ for $t \leq x$, and the piecewise continuous variation of velocities and stresses $v_a(x, t) = -\sigma^a(x, t) = 1$ for $t \geq x$ and $v_a(x, t) = \sigma^a(x, t) = 0$ for $t \leq x$ (at the interface $x = t$, jumps in stresses and velocities occur). The observation time is chosen to be $T = 18$. During this time the velocity pulse travels within the bar with two reflections from each end of the bar.

It is known that the application of traditional semi-discrete methods to this problem leads to oscillations in velocities and stresses due to the spurious high-frequency response [19,22,28]. As we will see (e.g., from Fig. 2(b) and (c)), the finite elements with reduced numerical dispersion reduce these oscillations after basic computations but they do not completely remove them from the numerical solution. Therefore, the two-stage procedure with the filtering stage as described in the Appendix will be applied for accurate and non-oscillatory solutions. The 1-D impact problem with propagating discontinuities in stresses and velocities can be considered a good benchmark problem for the testing of new numerical methods for wave propagation problems.

The problem is solved on uniform meshes with 100 and 300 linear two-node finite elements with the lumped and averaged ($\gamma = \frac{3-t^2}{2}$) mass matrices using the standard explicit central difference method in time based on Eq. (4) (for the lumped

mass matrix $\mathbf{M} = \mathbf{D}$, Eq. (4) reduces to the standard form of the explicit central difference method). We will consider very small time increments $\Delta t = t^{\text{st}}/20$ (much smaller than the stability limit Δt^{st} ; e.g., $\Delta t^{\text{st}} = 0.04$ and $\Delta t^{\text{st}} = 0.013333$ for uniform meshes with 100 and 300 linear finite elements, respectively). Very small time increments for the 1-D problems are the worst case from the point of view of accuracy because at basic computations for the time increments equal to the stability limit, the numerical solutions on uniform meshes with linear elements coincide with the exact solution; see Section 2.1.

We should also mention that the techniques based on the modified integration rule with $\alpha_M = \sqrt{\frac{4-\tau^2}{3}}$ and on the averaged mass matrix with $\gamma = \frac{3-\tau^2}{2}$ are completely equivalent and yield the same results in the 1-D case; see Section 2.1.

Fig. 2 shows the numerical results obtained by the linear elements with the lumped and averaged mass matrices after basic computations with very small time increments $\Delta t = t^{\text{st}}/20$ and after the filtering stage (post-processing). The use of the formulation with the reduced dispersion error (see curve 2 in Fig. 2(b) and (c)) reduces the amplitudes of spurious oscillations and yields a more accurate slope of the wave front at $x = 2$ compared with those for the lumped mass matrix at the same numbers of elements (see curve 3 in Fig. 2(b) and (c)). However, the presence of spurious high-frequency oscillations makes it difficult to compare the numerical results. After the filtering of spurious oscillations, we can see that for the selected observation time $T = 18$ and at the same accuracy, the use of the averaged mass matrix reduces the number of degrees of freedom by a factor of three as compared with that for the standard lumped mass matrix (see curves 2 and 3 in Fig. 3). We should mention that with the increase in the observation time, the difference in accuracy between the linear elements with reduced dispersion and the standard linear elements increases; i.e., the efficiency of the linear elements with reduced dispersion increases with the increase in the observation time (see curves 2 and 3 in Fig. 3(c)–(f) at the observation times $T = 18$ and $T = 194$). It is also interesting to note that the linear elements with reduced dispersion used with the implicit (as in our paper [18]) and explicit (as in the current paper) time-integration methods with very small time increments yield

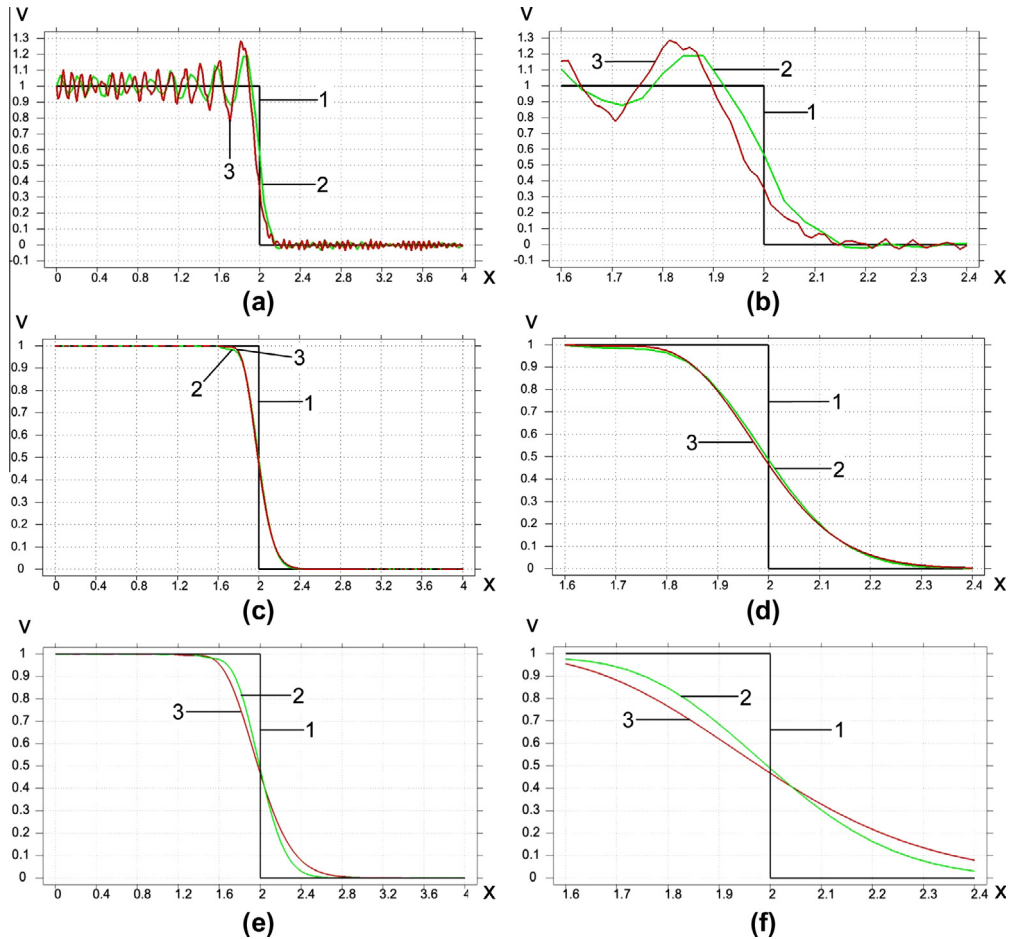


Fig. 3. The velocity distribution along the bar at observation times $T = 18$ (a-d) and $T = 194$ (e,f) after basic computations with small time increments $\Delta t = \Delta t^{\text{st}}/20$ (a, b) and after the filtering stage (c-f). Curves 1 correspond to the analytical solution. Curves 2 correspond to the numerical solutions with the averaged ($\gamma = \frac{3-\tau^2}{2}$) mass matrix on a uniform mesh with 100 linear 2-node finite elements. Curves 3 correspond to the numerical solutions with the lumped mass matrix on a uniform mesh with 300 linear 2-node finite elements. (b), (d), and (f) show the zoomed graphs (a), (c) and (e) in the range $1.6 < x < 2.4$.

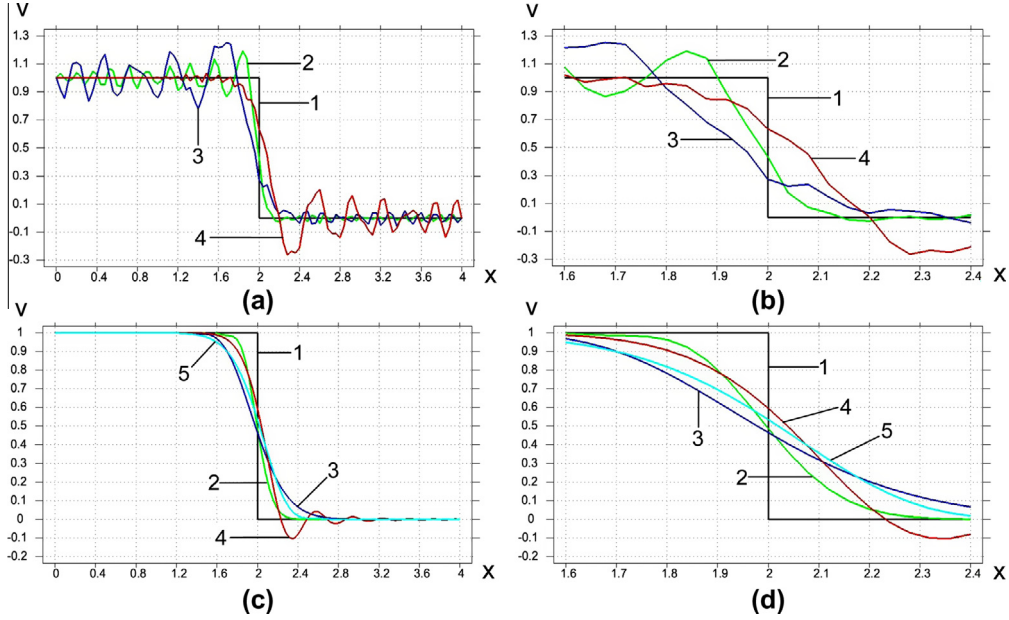


Fig. 4. The velocity distribution along the bar at observation time $T = 18$ after basic computations (a, b) and after the filtering stage (c, d). A uniform mesh with 100 linear 2-node finite elements is used. Curves 1 correspond to the analytical solution. Curves 2 and 3 correspond to the numerical solutions with the averaged ($\gamma = \frac{3-\tau^2}{2}$) and lumped mass matrices (with small time increments $\Delta t = \Delta t^{st}/20$ in basic computations). Curves 4 correspond to the numerical solutions for the averaged ($\gamma = 1.5$) mass matrix and the time increments close to the stability limit in basic computations. (b) and (d) show the zoomed graphs (a) and (c) in the range $1.6 < x < 2.4$. Curves 4 and 5 in (c) and (d) differ by the amount of numerical dissipation used at the filtering stage; see the text.

similar results at the stage of basic computations and after the filtering stage; see curves 2 and 4 in Fig. 2 (curves 4 for the implicit method is slightly more accurate than curves 2 for the explicit method). The analysis of the dispersion error in the 1-D case for averaged mass matrix technique shows (see Section 2 and our paper [18]) that despite the same order of accuracy, the leading term for the dispersion error is slightly smaller for the implicit method than that for the explicit method.

In Fig. 4, we have also analyzed the numerical results for the averaged mass matrix with $\gamma = \frac{3}{2}$ (as suggested in [5]) and the explicit central difference method with time increments close to the stability limit at basic computations. As we can see, in this case the results after basic computations (curve 4 in Fig. 4(a) and (b)) are less accurate than those described by curve 2 in Fig. 4(a) and (b). If we filter these results (curve 4 in Fig. 4(a) and (b)) with the amount of numerical dissipation (time increments) used for curve 2 in Fig. 4(a) and (b), then spurious oscillations remain after the filtering stage (curve 4 in Fig. 4(c) and (d)). If we use a sufficient amount of numerical dissipation at the filtering stage then the results (curve 5 in Fig. 4(c) and (d)) are close to curve 3 in Fig. 4(c) and (d). This means that the approach suggested in [5] for the averaged mass matrix does not improve the dispersion error and the accuracy of numerical results if relative large time increments (close to the stability limit) are used in calculations. However, at small time increments $\Delta t \approx 0$, parameter $\tau \approx 0$ is also small and $\gamma = \frac{3-\tau^2}{2} \approx \frac{3}{2}$; i.e., the results for $\gamma = \frac{3}{2}$ will coincide with curve 2 in Fig. 4 at small time increments in basic computations.

It is also interesting to note that because the numerical solutions with the implicit (see our paper [18]) and explicit (as in the current paper) time-integration methods for the linear elements with reduced dispersion are similar (see curves 2 and 4 in Fig. 2), then some conclusions from our paper [18] are also applicable to the linear elements with reduced dispersion and explicit time-integration methods. E.g., after the filtering stage, the numerical results obtained with the averaged mass matrix $\gamma = \frac{3-\tau^2}{2}$ (or the modified integration rule with $\alpha_M = \sqrt{\frac{4-\tau^2}{3}}$) converge to the analytical solution at mesh refinement (similar to the results in [18]). The linear elements with the reduced dispersion and the explicit time-integration methods are more accurate than the standard quadratic elements with the consistent mass matrix (similar to the results in [18]). Similar to the results in [18], the range of frequencies included in numerical solutions after the filtering stage is indirectly determined by the size of the time increments calculated by Eqs. (A.1)–(A.3) (see the Appendix). The numerical results show that if the time increments calculated according to Eqs. (A.1)–(A.3) for the filtering stage are close to each other for the formulations with the lumped, consistent or averaged mass matrices on different uniform meshes, then the numerical solutions obtained on these different uniform meshes are close to each other. This means that Eqs. (A.1)–(A.3) allow the quantitative estimation of the advantage of the averaged mass matrix ($\gamma = \frac{3-\tau^2}{2}$) compared with the standard approaches with the lumped and consistent mass matrices. For example, at the integration by the explicit central-difference method with very small time increments, for a uniform mesh with 100 linear finite elements and the averaged mass matrix ($\gamma = \frac{3-\tau^2}{2}$), the size of the time increments at the filtering stage is $\Delta t_1 = 0.04083$ according to Eqs. (A.1) and (A.2). For a uniform mesh with 300 linear finite elements and the lumped mass matrix, the size of the time increments at the filtering stage is $\Delta t_2 = 0.04075$ according to

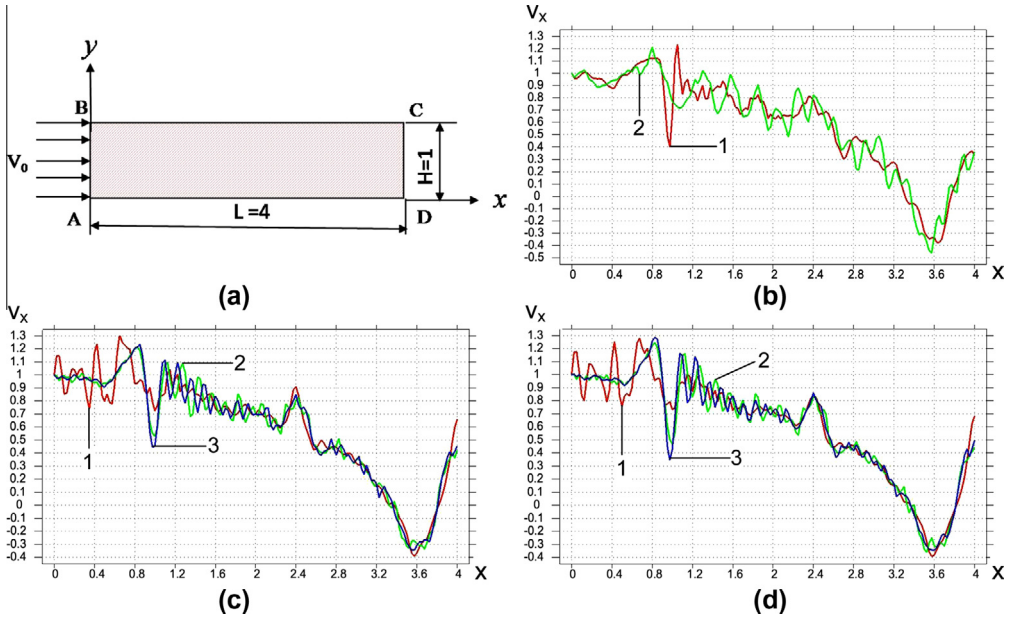


Fig. 5. A 2-D plane strain impact problem (a). The axial velocity distribution along the axis of symmetry AD at observation time $T = 13$ for the Poisson's ratio $\nu = 0.3$. The results are shown after basic computations and are obtained by the explicit central difference method with the lumped mass matrix (b), with the modified integration rule (c), and with the averaged mass matrix (d). Curves 1 and 2 correspond to the numerical solutions obtained with the time increments Δt^{st} and $\Delta t^{\text{st}}/20$, respectively. Curves 3 correspond to the numerical solutions (from our paper [18]) obtained by the implicit time-integration method with the modified integration rule (c) and the averaged mass matrix (d). A uniform mesh with $40 \times 160 = 6400$ linear 4-node finite elements is used.

Eqs. (A.1) and (A.2). Because Δt_2 is close to Δt_1 , then curves 2 and 3 in Fig. 3(c) and (d) are close to each other; see also the analytical solution, curve 1.

3.2. 2-D impact of an elastic bar against a rigid wall (plane strain)

This problem is a more general plane strain formulation of the 1-D impact problem considered in Section 3.1; see Fig. 5(a). In contrast to the 1-D impact problem, compressional and shear elastic waves propagate in the 2-D case.

A bar of length $L = 4$ and height $2H = 2$ is considered. Due to symmetry, the problem is solved for a half of the bar $ABCD$ where AD is the axis of symmetry. Young's modulus is chosen to be $E = 1$ and the density to be $\rho = 1$. Three cases of different Poisson's ratios $\nu = 0.1$, $\nu = 0.3$ and $\nu = 0.49$ are studied. The following boundary conditions are applied: along boundary AB $u_n = t$ (it corresponds to velocity $v_n = v_0 = 1$) and $\tau_n = 0$; along boundaries BC and CD $\sigma_n = 0$ and $\tau_n = 0$; along boundary AD $u_n = 0$ and $\tau_n = 0$, where u_n , v_n , and σ_n are the normal displacements, velocities and the tractive forces, respectively; τ_n are the tangential tractive forces. Initial displacements and velocities are zero; i.e., $u(x, y, 0) = v(x, y, 0) = 0$. The observation time is chosen to be $T = 13$. During this time the velocity pulse travels within the bar with multiple reflections from the ends of the bar and from the boundaries BC and AD .

The problem is solved on uniform coarse and fine meshes with linear four-node quadrilateral finite elements with the modified integration rule for the mass and stiffness matrices ($\alpha_M = \sqrt{\frac{4-\gamma^2}{3}}$ and $\alpha_K = \sqrt{\frac{4(2\nu-1)}{3(4\nu-3)}}$) and with the lumped and averaged ($\gamma = \frac{3-\gamma^2}{2}$) mass matrices. In order to study the effect of time increments at basic calculations on the accuracy of numerical results, we will use the time increments $\Delta t \approx \Delta t^{\text{st}}$ close to the stability limit Δt^{st} and smaller than the stability limit ($\Delta t = 0.5\Delta t^{\text{st}}$ and very small time increments $\Delta t = \Delta t^{\text{st}}/20$).

Figs. 5–10 show the distribution of the axial velocity along the axis of symmetry AD at observation time $T = 13$ for Poisson's ratio $\nu = 0.3$ after basic computations (Fig. 5) and for Poisson's ratios $\nu = 0.1$, $\nu = 0.3$ and $\nu = 0.49$ after the filtering stage (Figs. 6–10). Similar to the previous 1-D impact problem, the numerical results after basic computations with the lumped mass matrix and the formulations with reduced numerical dispersion contain spurious oscillations at very small time increments $\Delta t = \Delta t^{\text{st}}/20 = \frac{dx}{20c_1}$; see curves 2 in Fig. 5. However, in contrast to the 1-D impact problem, at basic computations the spurious oscillations and the dispersion error do not disappear for the time increments close to the stability limit; see curves 1 in Fig. 5. This is explained by the fact that we cannot zero the coefficients a_6 for the dispersion error simultaneously for the compressive ($c = c_1$) and shear ($c = c_2$) waves; see Section 2.2. It can be also seen from Fig. 5 (see curves 1 and 2) that the results after basic computation for the time increments close to the stability limit and for very small time increments are different for all methods. We should also note that at very small time increments, the numerical solutions

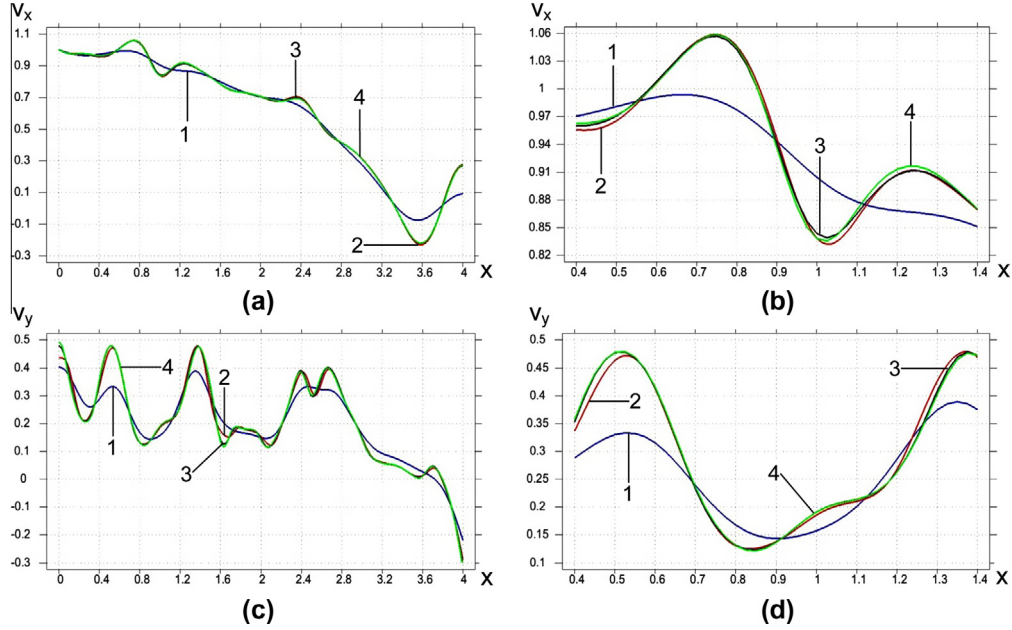


Fig. 6. The axial velocity distribution v_x along the axis of symmetry AD (a, b) and the transverse velocity distribution v_y along the external surface BC (c, d) at observation time $T = 13$ for the Poisson's ratio $\nu = 0.3$. The results are shown after the filtering of the solutions obtained at basic computations by the explicit central difference method with the lumped mass matrix (curves 1 and 2), with the modified integration rule (curve 3), and with the averaged mass matrix (curve 4). Small time increments $\Delta t^{\text{st}}/20$ are used at basic computations (see Fig. 5). Uniform meshes with $40 \times 160 = 6400$ (curves 1, 3 and 4) and $120 \times 480 = 57600$ (curve 2) linear elements are used. (b) and (d) show the zoomed graphs (a) and (c) in the range $0.4 < x < 1.4$.

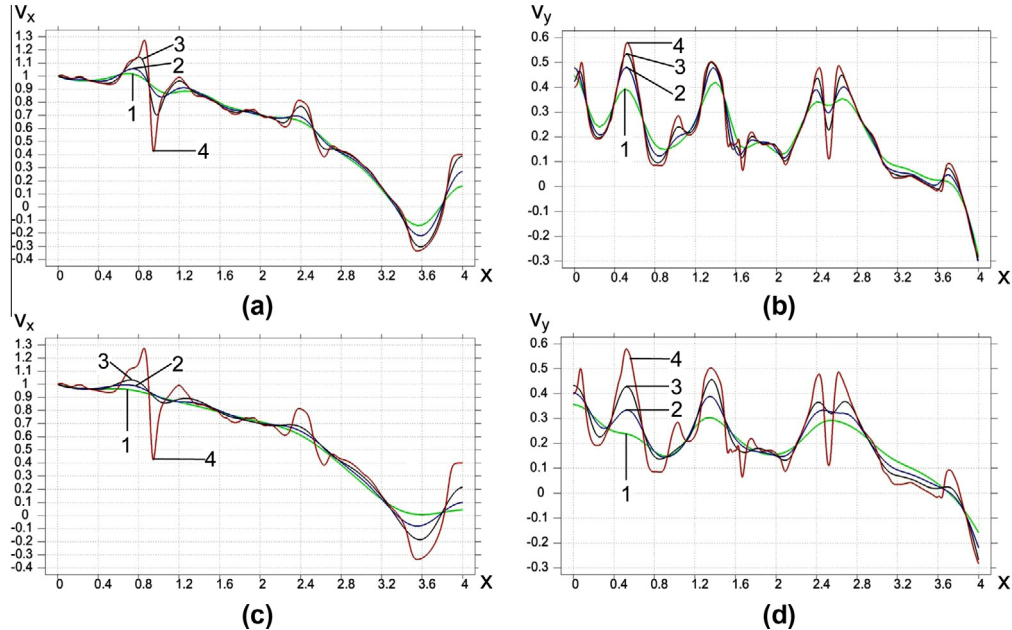


Fig. 7. The axial velocity distribution v_x along the axis of symmetry AD (a, c) and the transverse velocity distribution v_y along the external surface BC (b, d) at observation time $T = 13$ for the Poisson's ratio $\nu = 0.3$. The results are shown after the filtering of the solutions obtained at basic computations by the explicit central difference method with the modified integration rule (a, b) and with the standard approach (curves 1–3 in (c, d)). Small time increments $\Delta t^{\text{st}}/20$ are used at basic computations. Curves 1, 2, 3, 4 correspond to uniform meshes with $20 \times 80 = 1600$, $40 \times 160 = 6400$, $80 \times 320 = 25600$, and $320 \times 1280 = 409600$ linear elements. Curves 4 in (a, b, c, d) correspond to the modified integration rule and are considered as a reference solution.

for the linear elements with reduced dispersion obtained with the explicit central difference method (curves 2 in Fig. 5(c) and (d)) and with the implicit trapezoidal rule (see our paper [18] as well as curves 3 in Fig. 5(c) and (d)) are close to each

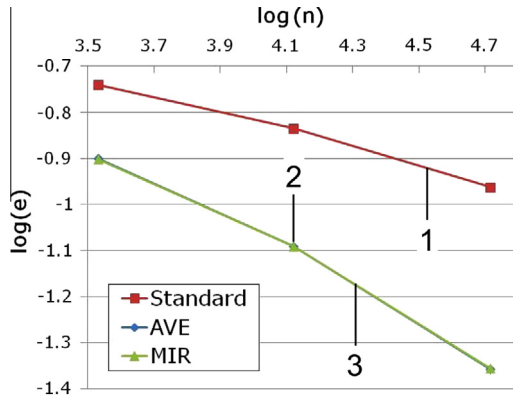


Fig. 8. The error in velocity e versus the number of degrees of freedom for the standard approach (curve 1), for the modified integration rule technique (curve 2) and for the averaged mass matrix technique (curve 3). The logarithmic scale is used. Curve 2 and 3 practically coincide.

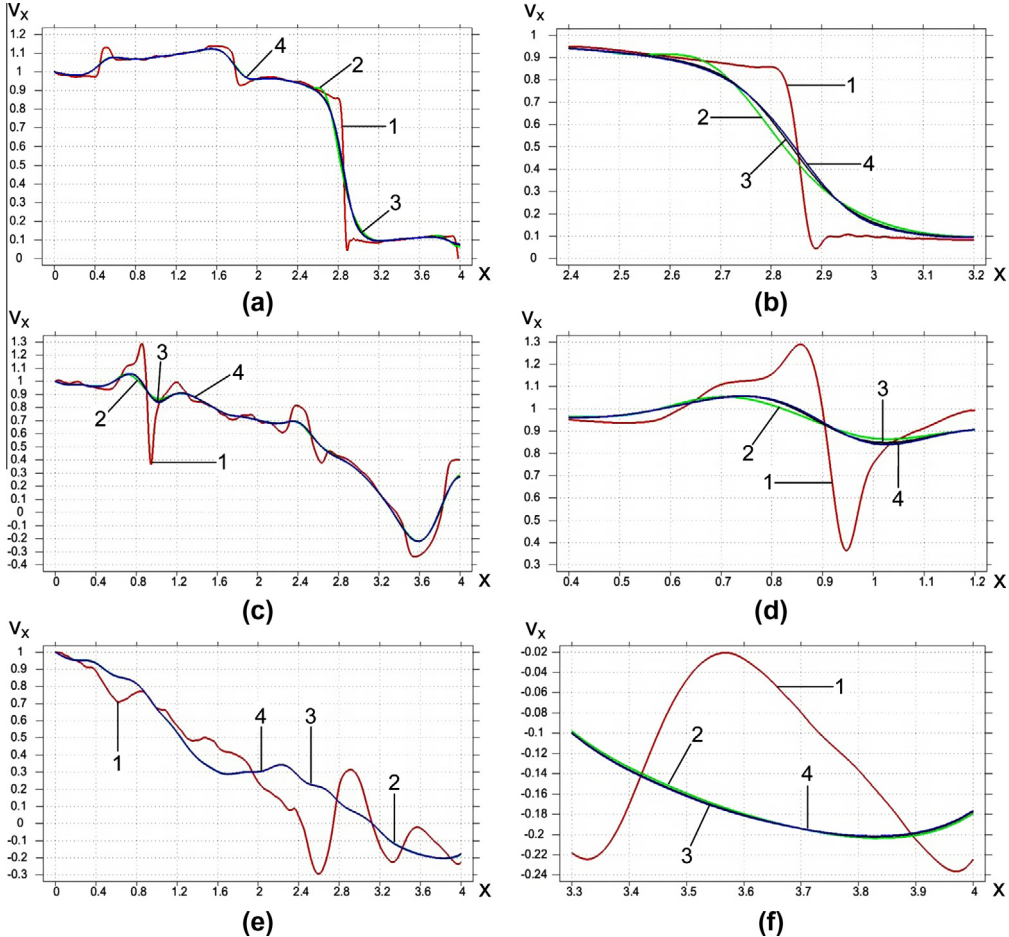


Fig. 9. The axial velocity distribution along the axis of symmetry AD at observation time $T = 13$ for the Poisson's ratios $\nu = 0.1$ (a, b), $\nu = 0.3$ (c, d) and $\nu = 0.49$ (e, f). The results are shown after the filtering of the solutions obtained at basic computations by the explicit central difference method with the modified integration rule and the following time increments: Δt^{st} (curves 2), $0.5\Delta t^{\text{st}}$ (curves 3) and $\Delta t^{\text{st}}/20$ (curves 4). A uniform mesh with $40 \times 160 = 6400$ linear 4-node finite elements is used. Curves 1 are the reference solutions (from our paper [18]) obtained by the implicit time-integration method with the modified integration rule on a fine mesh with $300 \times 1200 = 360000$ linear finite element. (b), (d) and (f) show the zoomed graphs (a), (c) and (e), respectively.

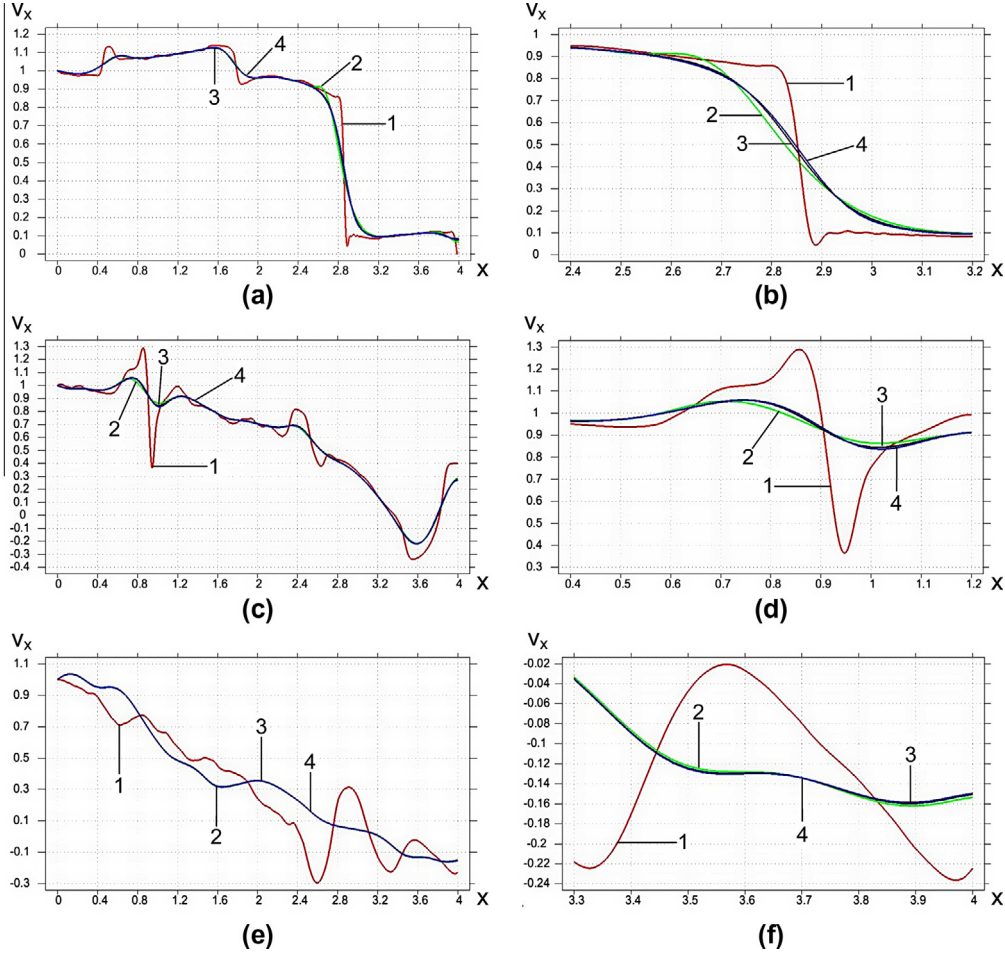


Fig. 10. The axial velocity distribution along the axis of symmetry AD at observation time $T = 13$ for the Poisson's ratios $\nu = 0.1$ (a, b), $\nu = 0.3$ (c, d) and $\nu = 0.49$ (e, f). The results are shown after the filtering of the solutions obtained at basic computations by the explicit central difference method with the averaged mass matrix and the following time increments: Δt^{st} (curves 2), $0.5\Delta t^{st}$ (curves 3) and $\Delta t^{st}/20$ (curves 4). A uniform mesh with $40 \times 160 = 6400$ linear 4-node finite elements is used. Curves 1 are the reference solutions (from our paper [18]) obtained by the implicit time-integration method with the averaged mass matrix on a fine mesh with $300 \times 1200 = 360000$ linear finite element. (b), (d) and (f) show the zoomed graphs (a), (c) and (e), respectively.

other. However, it is difficult to compare the accuracy of different approaches after basic computations due to large spurious oscillations.

After filtering spurious oscillations at the filtering stage, the solutions obtained at basic computations by the explicit central difference method at very small time increments $\Delta t^{st}/20$ with the modified integration rule (curves 3 in Fig. 6) and with the averaged mass matrix (curves 4 in Fig. 6) are close to each other. The results in Fig. 6 show that despite the impact along the x -axis, elastic waves propagate in all directions and the magnitudes of the transverse velocity v_y are comparable with those for the axial velocity v_x ; i.e., a general case of propagation of elastic waves occurs for the considered problem. As can be seen from Fig. 6, after the filtering stage the results obtained by the explicit central difference method at very small time increments $\Delta t^{st}/20$ and the lumped mass matrix (curves 1) are much less accurate than those obtained with the elements with reduced dispersion (curves 3 and 4). The results obtained by the standard approach on a fine mesh with $120 \times 480 = 57600$ linear elements (curves 2 in Fig. 6) show that at the selected observation time, the elements with reduced dispersion reduce the number of degrees of freedom by a factor of 9 compared with those for the standard approach at the same accuracy (compare curves 3 or 4 for a mesh with $40 \times 160 = 6400$ linear elements and curves 2 for a mesh with $120 \times 480 = 57600$ linear elements in Fig. 6).

Remark. Similar to the 1-D case in Section 3.1 and the results reported in our paper [18] for implicit time-integration methods, the size of the time increments calculated by Eqs. (A.1)–(A.3) for the filtering stage allows the quantitative estimation of the advantage of the modified integration rule (or the averaged mass matrix) technique compared with the standard lumped mass matrix. For example, for a uniform mesh with $40 \times 160 = 6400$ linear finite elements and the modified integration rule (or the averaged mass matrix), the size of the time increments at the filtering stage is $\Delta t_1 = 0.038204$ according to Eqs. (A.1)–(A.3). For a uniform mesh with $120 \times 480 = 57600$ linear finite elements and the lumped mass matrix, the size

of the time increments at the filtering stage is $\Delta t_2 = 0.036717$ according to Eqs. (A.1)–(A.3). Because Δt_2 is close to Δt_1 , then curves 2 and 3 (or 4) in Fig. 6 are close to each other. We should also mention that with the increase in the observation time, the efficiency of the elements with reduced dispersion increases compared with that for the standard approach; i.e., according to Eqs. (A.1)–(A.3), for the same accuracy of numerical results, the ratio $\frac{N_{FE}^{lump}}{N_{FE}^{red}}$ is an increasing function of the observation time (N_{FE}^{lump} and N_{FE}^{red} are the numbers of finite elements used with the standard formulation and with the formulations with reduced dispersion).

The convergence of the numerical results obtained at mesh refinement by the linear elements with the modified integration rule technique and by the standard approach is shown in Fig. 7 (the results are presented after the filtering stage). Uniform meshes with $20 \times 80 = 1600$, $40 \times 160 = 6400$, $80 \times 320 = 25600$, and $320 \times 1280 = 409600$ linear elements are used. Fig. 7 shows that for any mesh, the modified integration rule technique yields much more accurate solutions than the standard approach. We do not include the results for the averaged mass matrix technique because they are very close to those for the modified integration rule technique in Figs. 7(a) and (b). In order to quantify the analysis of convergence for different techniques, we introduce the following relative error in velocity:

$$e = \frac{\sqrt{\sum_{k=1}^m [\nu_x(k) - \nu_x^{ref}(k)]^2 + [\nu_y(k) - \nu_y^{ref}(k)]^2}}{\sqrt{\sum_{k=1}^m [\nu_x^{ref}(k)]^2 + [\nu_y^{ref}(k)]^2}}, \quad (43)$$

where $\nu_x(k)$ and $\nu_y(k)$ are the x - and y -components of the nodal velocity at node k , superscript “ref” designates the reference solution, $m = 1701$ is the total number of nodes of the coarse mesh with $20 \times 80 = 1600$ elements. In order to simplify the calculation of the error in Eq. (43) for different meshes, we use only nodes that are common for all meshes and correspond to the nodes of the coarse mesh with $20 \times 80 = 1600$ elements. Because for the 2-D impact problem we do not have the analytical solution then the numerical results obtained on the finest mesh with the $320 \times 1280 = 409600$ linear elements with reduced dispersion are used as a reference solution in Eq. (43). Fig. 8 shows the error e versus the number of degrees of freedom n for the standard linear elements (curve 1) and the linear elements with reduced dispersion (curves 2 and 3) using the logarithmic scale. The numerical results in Fig. 8 converge at mesh refinement and the relative error in velocity e approaches zero. It can be seen from Fig. 8 that the dispersion reduction techniques based on the modified integration rule and on the averaged mass matrix yield approximately the same results for elastodynamics problems (curves 2 and 3 in Fig. 8 practically coincide). We can also see that these techniques significantly reduce the number of degrees of freedom compared with that for the standard linear finite elements at the same accuracy; e.g., at accuracy $\log e \approx -0.9$ this reduction is approximately equal to a factor of 9 (see curves 1 and 2 at $\log e \approx -0.9$).

Figs. 9 and 10 show the effect of the size of time increments in basic computations on the accuracy of the results with the new formulations for different Poisson’s ratios. As can be seen, the results at very small time increments $\Delta t^{st}/20$ (curves 4) are more accurate than those at the time increments close to the stability limit Δt^{st} (curves 2); see also the reference solution (curves 1) from our paper [18] obtained by the implicit time-integration method with the modified integration rule on a fine mesh with $300 \times 1200 = 360000$ linear finite elements (the modified integration rule on a fine mesh with $320 \times 1280 = 409600$ linear finite elements and explicit time integration yields approximately the same reference solution; e.g., see curve 4 in Fig. 7 and curve 1 in Fig. 9(c)). This means that in contrast to the standard approach with the explicit central difference method (for which the time increments close to the stability limit yield more accurate results), very small time increments (much smaller than the stability limit) yield more accurate results for the formulations with reduced dispersion in the 2-D case (see also analysis in Section 2.2). It is also necessary to note that small time increments $0.5\Delta t^{st}$ (curves 3) and $\Delta t^{st}/20$ (curves 4) yield practically the same results for the formulations with the reduced dispersion; i.e., from the computational point of view, the time increments $0.5\Delta t^{st}$ can be recommended for these new formulations.

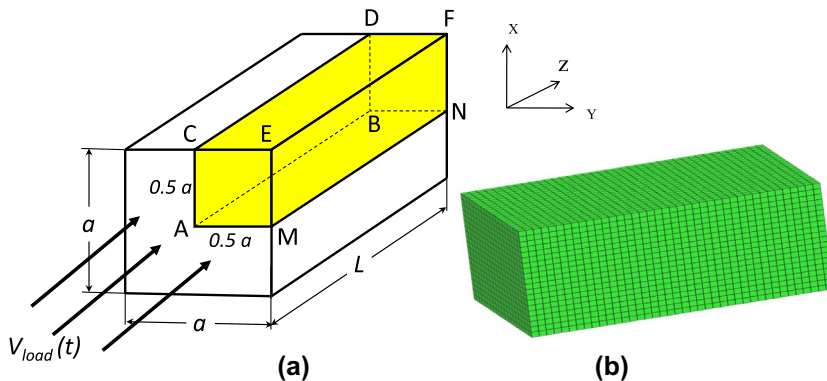


Fig. 11. Impact of an elastic 3-D square bar of length $L = 2$ and width $a = 2$ against a rigid wall (a). A uniform mesh with $20 \times 20 \times 40 = 16000$ linear Q finite elements is used (b).

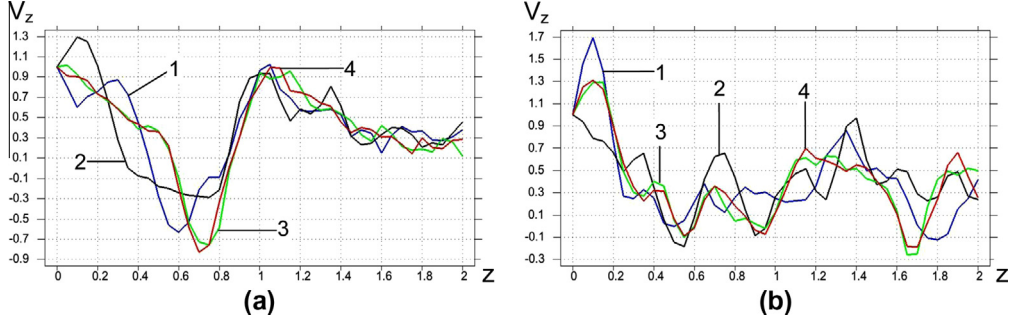


Fig. 12. The distribution of the axial v_z velocity component along lines EF (a) and AB (b) (see Fig. 11) after basic computations at time $T = 7$ on a uniform mesh with $20 \times 20 \times 40 = 16000$ linear Q8 finite elements. The Poisson's ratio is $\nu = 0.3$. The results are obtained by the explicit central difference method with the lumped mass matrix (curves 1 and 2), with the averaged mass matrix (curves 3), and with the modified integration rule (curves 4). The following time increments are used: Δt^{st} (curves 1) and $\Delta t^{\text{st}}/20$ (curves 2–4).

Figs. 9 and 10 also show that after the filtering stage, the difference between the numerical results obtained with the modified integration rule and the averaged mass matrix is small at different Poisson's ratios. This difference is slightly larger at Poisson's ratio close to 0.5. But even in this case it can be neglected compared with the change in the numerical results at mesh refinement (see curves 1 in Figs. 9 and 10).

3.3. 3-D impact of an elastic bar against a rigid wall

A solid 3-D bar of length $L = 2$ with a square cross section $a \times a$ ($a = 2$) under impact loading at the left end ACEM is considered; see Fig. 11. Due to symmetry, the problem is solved for a quarter of the bar ACEMNFD where planes ABDC and ABNM are the planes of symmetry. Young's modulus is chosen to be $E = 1$, Poisson's ratio to be $\nu = 0.3$, and the density to be $\rho = 1$. The following boundary conditions are applied: along the left end ACEM: $u_n = t$ (which corresponds to the instantaneous application of velocity $v_{\text{load}}(t) = v_0 = 1$) and $\tau_n = 0$; along planes BDFN, CDFE and EFNM: $\sigma_n = 0$ and $\tau_n = 0$ (free surfaces); along planes ABDC, ABNM: $u_n = 0$ and $\tau_n = 0$ where u_n , v_n , and σ_n are the normal displacements, velocities and the tractive forces, respectively; τ_n are the tangential tractive forces. The observation time is chosen to be $T = 7$. During

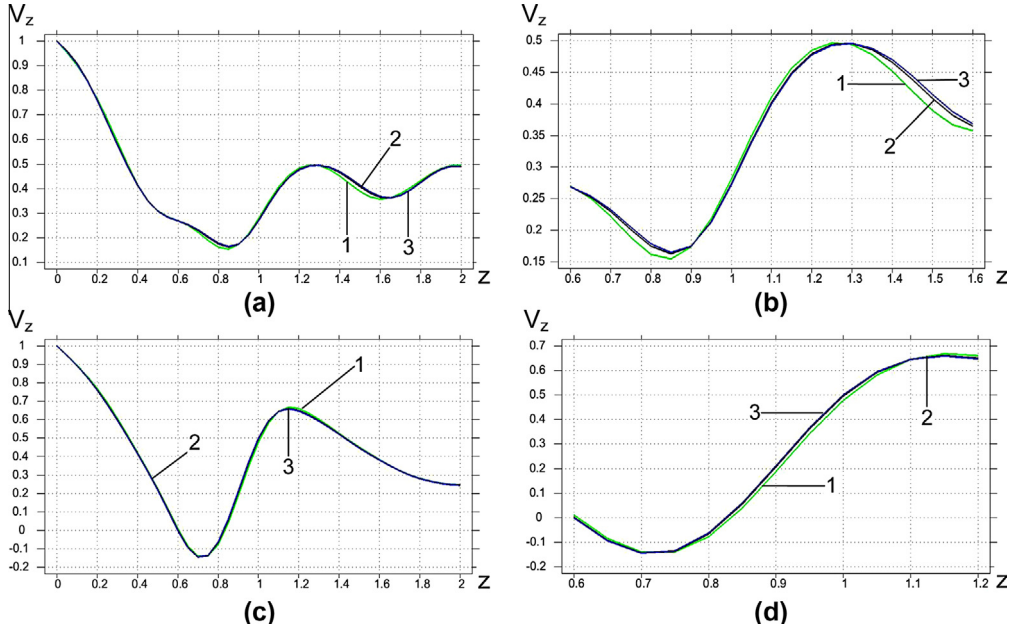


Fig. 13. The distribution of the axial v_z velocity component along lines AB (a, b) and EF (c, d) (see Fig. 11) at time $T = 7$ on a uniform mesh with $20 \times 20 \times 40 = 16000$ linear Q8 finite elements. The Poisson's ratio is $\nu = 0.3$. The results are shown after the filtering of the solutions obtained at basic computations by the explicit central difference method with the averaged mass matrix and the following time increments: Δt^{st} (curves 1), $0.5\Delta t^{\text{st}}$ (curves 2) and $\Delta t^{\text{st}}/20$ (curves 3). (b) and (d) show the zoomed graphs (a) and (c), respectively.

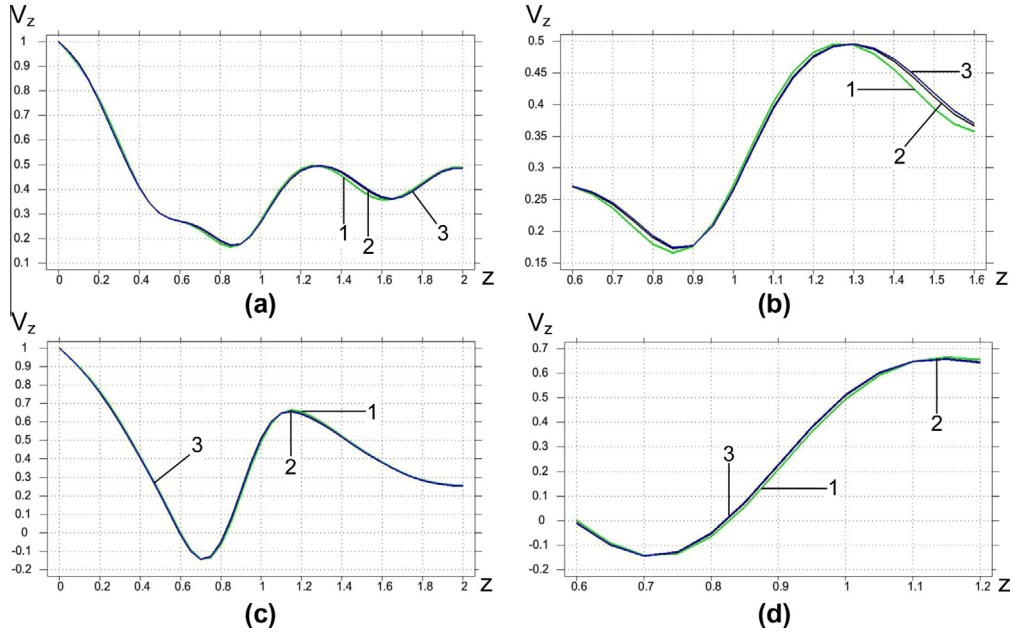


Fig. 14. The distribution of the axial v_z velocity component along lines AB (a, b) and EF (c, d) (see Fig. 11) at time $T = 7$ on a uniform mesh with $20 \times 20 \times 40 = 16000$ linear Q8 finite elements. The Poisson's ratio is $\nu = 0.3$. The results are shown after the filtering of the solutions obtained at basic computations by the explicit central difference method with the modified integration rule and the following time increments: Δt^{st} (curves 1), $0.5\Delta t^{\text{st}}$ (curves 2) and $\Delta t^{\text{st}}/20$ (curves 3). (b) and (d) show the zoomed graphs (a) and (c), respectively.

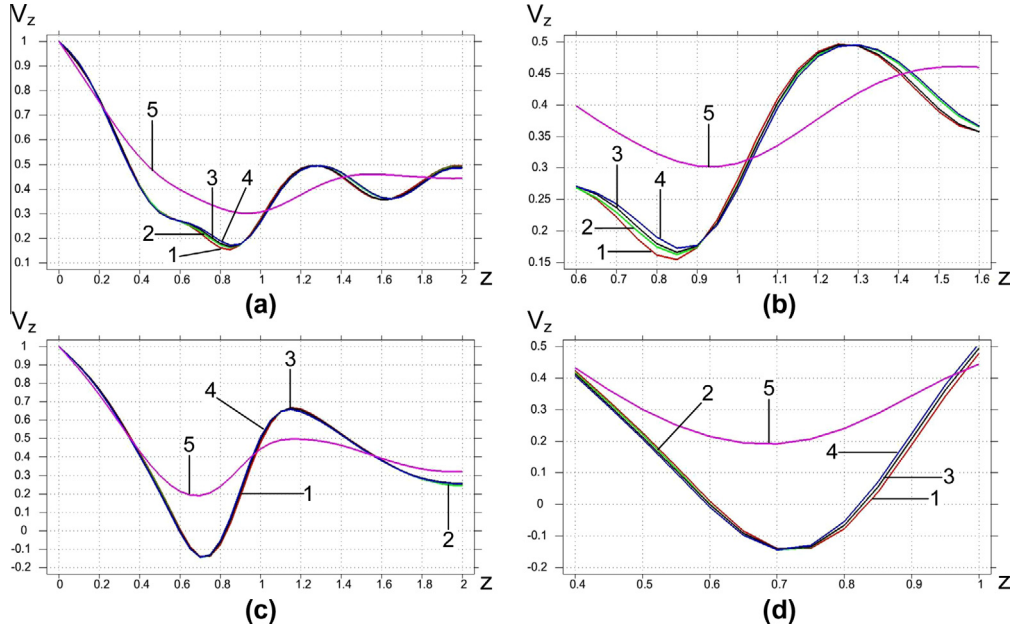


Fig. 15. The distribution of the axial v_z velocity component along lines AB (a, b) and EF (c, d) (see Fig. 11) at time $T = 7$ on a uniform mesh with $20 \times 20 \times 40 = 16000$ linear Q8 finite elements. The Poisson's ratio is $\nu = 0.3$. The results are shown after the filtering of the solutions obtained at basic computations by the explicit central difference method with the averaged mass matrix (curves 1 and 2), with the modified integration rule (curves 3 and 4) and with the lumped mass matrix (curves 5) and the following time increments: Δt^{st} (curves 1 and 3), $0.5\Delta t^{\text{st}}$ (curves 2, 4 and 5). (b) and (d) show the zoomed graphs (a) and (c), respectively.

this time the velocity pulse travels within the bar with multiple reflections from the ends of the bar and from the external surfaces CDFE and EFNM. The problem is solved by the explicit central-difference method on a uniform mesh with $20 \times 20 \times 40 = 16000$ eight-node tri-linear hexahedral elements with the modified integration rule for the mass and

stiffness matrices ($\alpha_M = \sqrt{\frac{4-\tau^2}{3}}$ and $\alpha_K = \sqrt{\frac{4(2\gamma-1)}{3(4\gamma-3)}}$) as well as with the lumped and averaged ($\gamma = \frac{3-\tau^2}{2}$) mass matrices. The numerical results in Figs. 12–15 show the distribution of the axial velocity V_z along lines EF and AB (see Fig. 11) at the observation time $T = 7$.

Similar to the previous 1-D and 2-D impact problems, the numerical results after basic computations contain spurious oscillations for all formulations; see Fig. 12. For the standard approach with the lumped mass matrix, the solution with the time increments close to the stability limit Δt^{st} is more accurate than that with very small time increments $\Delta t^{st}/20$; e.g., see curves 1 and 2 in Fig. 12 (curve 1 is closer to more accurate results, curves 3 and 4, obtained by the use of the formulations with reduced dispersion).

Figs. 13–15 show the results after the filtering stage for the formulations with reduced dispersion as well as for the standard formulation with the lumped mass matrix. As can be seen from Figs. 13 and 14, the results obtained at basic computation at very small time increments $\Delta t^{st}/20$ (curves 3) and at the time increments close to the stability limit Δt^{st} (curves 1) are different for some intervals along the z axis. However, similar to the 2-D case, small time increments $0.5\Delta t^{st}$ (curves 2) and $\Delta t^{st}/20$ (curves 3) yield practically the same results for the formulations with the reduced dispersion; i.e., from the computational point of view, the time increments $0.5\Delta t^{st}$ can be recommended for these new formulations at basic computations. It can be also seen from Fig. 15 that at small time increments $0.5\Delta t^{st}$, the solutions obtained with the averaged mass matrix and with the modified integration rule are close to each other (similar to the 2-D case). The numerical solution for the standard formulation with the lumped mass matrix is less accurate on the same mesh; see curves 5 in Fig. 15. We should also mention that similar to the 1-D and 2-D cases, the size of the time increments calculated by Eqs. (A.1)–(A.3) for the filtering stage allows the quantitative estimation of the advantage of the modified integration rule (or the averaged mass matrix) technique compared with the standard lumped mass matrix in the 3-D case as well.

4. Concluding remarks

In our paper [18], we have described the finite element techniques with reduced dispersion for elastodynamics that are based on implicit time-integration methods with very small time increments. These techniques significantly reduce the computation time at the same accuracy compared with the standard finite element formulations with the consistent mass matrix. However, one of the disadvantages of the use of implicit time-integration methods is the necessity to solve a system of algebraic equations that can require large computational resources for a large number of degrees of freedom. In this paper we have extended the finite element techniques with reduced dispersion for elastodynamics that can be used with explicit time-integration methods. We have considered two techniques: one of them is based on the use of the averaged mass matrix; another is based on the modified integration rule for the mass and stiffness matrices. According to the analytical study of the numerical dispersion, the modified integration rule approach is more accurate than that based on the averaged mass matrix. However, numerical examples show that the difference between the numerical solutions obtained with these techniques is small and can be neglected. It is also interesting to note that at small time increments, the techniques with reduced dispersion based on implicit and explicit time-integration methods significantly reduce the number of degrees of freedom compared with the standard finite elements at the same accuracy (e.g., by a factor of 3 in the 1-D case and 9 in the 2-D case and 27 in the 3-D case, see Section 3 as well as our paper [18]). This leads to a huge reduction in the computation time. However, explicit methods yield an additional significant reduction in the computation time compared with implicit methods. In this paper we have also studied the effect of time increments on the accuracy of the numerical results. The analytical study and the numerical results show that in contrast to the standard approach with the explicit time-integration methods and the lumped mass matrix, the finite element techniques with reduced dispersion yield more accurate results at very small time increments (smaller than the stability limit Δt^{st}) in the 2-D and 3-D cases. Numerical experiments show that the numerical results on uniform meshes at small time increments $0.5\Delta t^{st}$ and $0.05\Delta t^{st}$ are close to each other. Therefore, from the computational point of view, the time increments $0.5\Delta t^{st}$ can be recommended for calculations. We should also mention that the formulations with reduced dispersion and the explicit time-integration methods can be directly and efficiently used (practically, without modifications) on parallel computers because the numerical algorithm includes the matrix and vector multiplications and can be performed at the element level without the solution of a system of algebraic equations.

The new finite element techniques with reduced numerical dispersion significantly increase the accuracy of numerical solutions for elastodynamics problems; however, they do not remove all spurious high-frequency oscillations for wave propagation problems. The spurious oscillations make it difficult to estimate the efficiency of these formulations applied to engineering elastodynamics problems. In the paper, this issue has been overcome by the use of the two-stage time-integration technique with the filtering stage [19,20,22], which quantifies and removes spurious oscillations. It is also interesting to mention that the amount of numerical dissipation at the filtering stage can be used as a quantitative measure for the comparison of accuracy of the standard finite element formulations and the formulations with reduced dispersion.

In the future, we plan to apply the finite elements with reduced dispersion to non-linear problems. Because the averaged matrix technique is independent of material properties we hope that it can be efficiently used for wave propagation problems in non-elastic materials.

Acknowledgments

The research has been supported in part by the Air Force Office of Scientific Research (contract FA9550-12-1-0324) and by Texas Tech University.

Appendix A. The two-stage time-integration technique with filtering spurious oscillations (see [19,20,22])

In order to filter spurious high-frequency oscillations, numerical dissipation (or artificial damping) is usually introduced for the time integration of Eq. (1). As we showed in our paper [22], the use of a time-integration method with numerical dissipation (or artificial damping) at each time increment leads to inaccurate numerical results for low frequencies as well, especially for a long-term integration. It is also unclear in this case how to select the amount numerical dissipation and the range of high frequencies to be filtered.

To resolve these issues, we have developed the two-stage time-integration technique (see [19,20,22]) with the stage of basic computations and the filtering stage. This technique is based on the fact that for linear elastodynamics problems, there is no necessity to filter spurious high-frequency oscillations at each time increment because the errors in high frequencies do not affect the accuracy of low frequencies during time integration; see [22]. In the current paper, we use the standard explicit central-difference time-integration method (without numerical dissipation or artificial viscosity) at basic computations in order to obtain an accurate solution of the semi-discrete elastodynamics problem, Eq. (1) (this solution contains spurious high-frequency oscillations). We should mention that other known explicit time-integration methods can be also used for basic computations (however, in this case the dispersion analysis of Section 2 should be modified for the corresponding explicit time-integration method). For the filtering of spurious oscillations, the implicit TCG method with large numerical dissipation developed in [22] is used at the filtering stage. For all elastodynamics problem, we use $N = 10$ uniform time increments (5 positive plus 5 negative time increments) at the filtering stage. This means that there is no real time integration at the filtering stage (the sum of 10 time increments used at the filtering stage is zero). As shown in [22], this procedure is equivalent to the multiplication of each velocity and displacement component of the uncoupled system of the semi-discrete equations by a factor of $\left(\frac{(3+m)^2+\Omega^2}{(3+m)^2+(2+m)^2\Omega^2}\right)^5$ (where $\Omega = \omega_j \Delta t$ and ω_j are the eigen-frequencies of the semi-discrete system, Δt is the time increment as well as $m = 15$ is used) and does not require the modal decomposition and the calculation of eigen-frequencies. As can be seen, this factor is close to zero for large Ω and is close to unity for small Ω . The size Δt of time increments at the filtering stage indirectly defines the amount of numerical dissipation and the range of spurious frequencies and is calculated according to the following formulas (for uniform meshes)

$$\Delta t = \alpha \left(\frac{c_o T}{dx} \right) \frac{dx \Omega_{0.1}(N)}{c_o}, \quad (\text{A.1})$$

with

$$\alpha \left(\frac{c_o T}{dx} \right) = a_1 \left(\frac{c_o T}{dx} \right)^{a_2}, \quad (\text{A.2})$$

in the 1-D case and

$$\begin{aligned} \Delta t &= \max_{m,j} \left[\alpha \left(\frac{c_m T}{dx_j} \right) \frac{dx_j}{c_m} \right] \Omega_{0.1}(N) = \max_{m,j} \left[\frac{dx_j}{c_m} \right]^{1-a_2} a_1 T^{a_2} \Omega_{0.1}(N) = \left[\frac{\max dx_j}{\min c_m} \right]^{1-a_2} a_1 T^{a_2} \Omega_{0.1}(N) \\ &= \left[\frac{dx_{\max}}{c_2} \right]^{1-a_2} a_1 T^{a_2} \Omega_{0.1}(N), \end{aligned} \quad (\text{A.3})$$

in the 2-D and 3-D cases (see our papers [20,22]). Here, $c_o = \sqrt{\frac{E}{\rho}}$ is the wave velocity; dx is the size of a finite element in the 1-D case; T is the observation time; $c_2 = \min c_m$ ($i = 1, 2$) is the minimum value between the velocities of the compressional wave c_1 and the shear wave c_2 (see Eq. (8)); $dx_{\max} = \max_j dx_j$ is the maximum dimension of finite elements along the axes x_j ($j = 1, 2$ for 2-D problems and $j = 1, 2, 3$ for 3-D problems); $\Omega_{0.1}(N = 10) = 0.81$ for the TCG method with $N = 10$ time increments. Eq. (A.3) is based on Eqs. (A.1) and (A.2) with the selection of the maximum size of a time increment with respect to the compressional and shear waves, and the maximum size of a finite element along the coordinate axes. Using the calibration procedure described in [20], we found the following coefficients a_1 and a_2 for the filtering stage: $a_1 = 0.3296$ and $a_2 = 0.218$ for the linear elements with the averaged $(\gamma = \frac{3-\tau^2}{2})$ mass matrix or the modified integration rule and the explicit time-integration method in basic computations as in the current paper; $a_1 = 0.2942$ and $a_2 = 0.2104$ for the linear elements with the averaged $(\gamma = \frac{3-\tau^2}{2})$ mass matrix or the modified integration rule and the implicit time-integration method in basic computations as in our paper [18]; $a_1 = 0.3342$ and $a_2 = 0.3363$ (see our paper [23]) for the standard explicit time integration with the linear elements and the lumped mass matrix. These coefficients a_1 and a_2 are calibrated in the 1-D case for the filtering of numerical results obtained at basic computations with very small time increments.

In order to use the same coefficients a_1 and a_2 in the 2-D and 3-D cases, small time increments should be used at basic computations for the 2-D and 3-D problems. However, as shown in Section 2, for the standard approach with the central-difference method and the lumped mass matrix, the time increments close to the stability limit yield more accurate results at basic computations than very small time increments do. Therefore, the minimum amount of numerical dissipation given by Eq. (A.3) is slightly conservative for the standard approach in the 2-D and 3-D cases if the time increments at basic computations are close to the stability limit. Nevertheless, in this case the numerical solutions obtained at basic computations at any time increments (close or smaller than the stability limit) are practically the same after the filtering based on Eq. (A.3). In contrast to the standard approach, for the 2-D and 3-D linear elements with reduced dispersion, small time increments (smaller than the stability limit Δt^{st}) should be used at basic computations ($0.5\Delta t^{\text{st}}$ can be recommended at basic computations; see Sections 2 and 3). We should also mention that the filtering stage can be applied in the beginning of calculations as a pre-processor, in the end of calculations as a post-processor or at some intermediate time (see [18,21–23] for numerous examples of the application of the two-stage time-integration technique).

References

- [1] H.P. Cherukuri, Dispersion analysis of numerical approximations to plane wave motions in an isotropic elastic solid, *Comput. Mech.* 25 (4) (2000) 317–328.
- [2] W. Dauksher, A.F. Emery, Solution of elastostatic and elastodynamic problems with Chebyshev spectral finite elements, *Comput. Methods Appl. Mech. Eng.* 188 (1) (2000) 217–233.
- [3] D. Gabriel, J. Plesek, R. Kolman, F. Vales, Dispersion of elastic waves in the contact-impact problem of a long cylinder, *J. Comput. Appl. Math.* 234 (2010) 1930–1936.
- [4] M.N. Guddati, B. Yue, Modified integration rules for reducing dispersion error in finite element method, *Comput. Methods Appl. Mech. Eng.* 193 (2004) 275–287.
- [5] S. Krenk, Dispersion-corrected explicit integration of the wave equation, *Comput. Methods Appl. Mech. Eng.* 191 (2001) 975–987.
- [6] K.J. Marfurt, Accuracy of finite difference and finite element modeling of the scalar and elastic wave equation, *Geophysics* 49 (1984) 533–549.
- [7] R. Mullen, T. Belytschko, Dispersion analysis of finite element semidiscretizations of the two-dimensional wave equation, *Int. J. Numer. Methods Eng.* 18 (1982) 11–29.
- [8] G. Seriani, S.P. Oliveira, Optimal blended spectral-element operators for acoustic wave modeling, *Geophysics* 72 (5) (2007) 95–106.
- [9] G. Seriani, S.P. Oliveira, Dispersion analysis of spectral element methods for elastic wave propagation, *Wave Motion* 45 (6) (2008) 729–744.
- [10] B. Yue, M.N. Guddati, Dispersion-reducing finite elements for transient acoustics, *J. Acoust. Soc. Am.* 118 (4) (2005) 2132–2141.
- [11] F.I. Zyserman, P.M. Gauzello, Dispersion analysis of a nonconforming finite element method for the three-dimensional scalar and elastic wave equations, *Finite Elem. Anal. Des.* 41 (13) (2005) 1309–1326.
- [12] T. Hughes, A. Real, G. Sangalli, Duality and unified analysis of discrete approximations in structural dynamics and wave propagation: comparison of p-method finite elements with k-method nurbs, *Comput. Methods Appl. Mech. Eng.* 197 (49–50) (2008) 4104–4124.
- [13] Z.C. He, A.G. Cheng, G.Y. Zhang, Z.H. Zhong, G.R. Liu, Dispersion error reduction for acoustic problems using the edge-based smoothed finite element method (es-fem), *Int. J. Numer. Methods Eng.* 86 (11) (2011) 1322–1338.
- [14] D. Wang, R. Tezaur, J. Toivanen, C. Farhat, Overview of the discontinuous enrichment method, the ultra-weak variational formulation, and the partition of unity method for acoustic scattering in the medium frequency regime and performance comparisons, *Int. J. Numer. Methods Eng.* 89 (4) (2012) 403–417.
- [15] I. Babuska, F. Ihlenburg, T. Strouboulis, S.K. Gangaraj, Posteriori error estimation for finite element solutions of helmholtz' equation – part ii: estimation of the pollution error, *Int. J. Numer. Methods Eng.* 40 (21) (1997) 3883–3900.
- [16] I. Babuska, T. Strouboulis, S.K. Gangaraj, C.S. Upadhyay, Pollution error in the h-version of the finite element method and the local quality of the recovered derivatives, *Comput. Methods Appl. Mech. Eng.* 140 (1–2) (1997) 1–37.
- [17] A. Deraemaeker, I. Babuska, P. Bouillard, Dispersion and pollution of the fem solution for the helmholtz equation in one, two and three dimensions, *Int. J. Numer. Methods Eng.* 46 (4) (1999) 471–499.
- [18] A. Idesman, M. Schmidt, J.R. Foley, Accurate finite element modeling of linear elastodynamics problems with the reduced dispersion error, *Comput. Mech.* 47 (2011) 555–572.
- [19] A.V. Idesman, A new high-order accurate continuous Galerkin method for linear elastodynamics problems, *Comput. Mech.* 40 (2007) 261–279.
- [20] A.V. Idesman, H. Samajder, E. Aulisa, P. Seshaiyer, Benchmark problems for wave propagation in elastic materials, *Comput. Mech.* 43 (6) (2009) 797–814.
- [21] A. Idesman, K. Subramanian, M. Schmidt, J.R. Foley, Y. Tu, R.L. Sierakowski, Finite element simulation of wave propagation in an axisymmetric bar, *J. Sound Vib.* 329 (2010) 2851–2872.
- [22] A.V. Idesman, Accurate time integration of linear elastodynamics problems, *Comput. Model. Eng. Sci.* 71 (2) (2011) 111–148.
- [23] A. Idesman, M. Schmidt, J.R. Foley, Accurate 3-d finite element simulation of elastic wave propagation with the combination of explicit and implicit time-integration methods, *Wave Motion* 48 (2011) 625–633.
- [24] T.J.R. Hughes, *The Finite Element Method: Linear Static and Dynamic Finite Element Analysis*, Prentice- Hall, Englewood Cliffs, NJ, 1987.
- [25] K.J. Bathe, *Finite Element Procedures*, Prentice-Hall Inc., Upper Saddle River, New Jersey, 1996.
- [26] W. Nowacki, *Dynamic Problems of Thermoelasticity*, Springer, 1975.
- [27] O.C. Zienkiewicz, R.L. Taylor, *The Finite Element Method*, Butterworth-Heinemann, Oxford, UK, 2000.
- [28] G.M. Hubert, T.J.R. Hughes, Space-time finite element methods for second-order hyperbolic equations, *Comput. Methods Appl. Mech. Eng.* 84 (3) (1990) 327–348.